Journal of Volcanology and Geothermal Research 347 (2017) 337–359

Contents lists available at ScienceDirect

Journal of Volcanology and Geothermal Research

journal homepage: www.elsevier.com/locate/jvolgeores

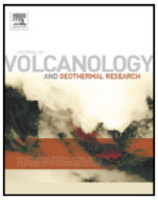

Episodic inflation and complex surface deformation of Akutan volcano, Alaska revealed from GPS time-series

Kimberly DeGrandpre [a],*, Teng Wang [a], Zhong Lu [a], Jeffrey T. Freymueller [b]

[a] *Huffington Department of Earth Sciences, Southern Methodist University, Dallas, TX, USA*
[b] *University of Alaska Fairbanks, Fairbanks, AK, USA*

ARTICLE INFO

Article history:
Received 7 March 2017
Received in revised form 20 June 2017
Accepted 6 October 2017
Available online 12 October 2017

Keywords:
Akutan volcano
GPS time-series
Surface deformation
Source modeling

ABSTRACT

Akutan is one of the most active volcanoes in the Aleutian island arc. Studies involving seismic, GPS, and InSAR data have observed activity and deformation on the island since 1996. In this study we inverted measurements of volcanic deformation, observed using three components of motions at 12 continuous GPS sites to define magma source parameters using Mogi point source, Okada dislocation, and Yang spheroid and ellipsoid models. In order to analyze the evolution of this magma source we split the GPS data into five consecutive time periods, and one period that incorporates all available data. These time periods were designed around two inflation events in 2008 and 2014, when a sudden and significant increase in vertical velocity was observed. Inversion of these time periods independently allowed us to create a magma volume time-series that is related to the physical migration of magma defined by the estimated source parameters. The best fit model parameters resulting from these inversions describes magma storage in the form of an oblate spheroid centered on the northeastern rim of the caldera of Akutan volcano, extending from a depth of 7 km to 8 km, with a length of ~3.5 km, a strike of ~N165°E, and a dip of ~63° from the horizontal to the southwest. Our model results were compared with seismic studies and found to support previous interpretations of episodic inflation beneath Akutan volcano with complicated magma storage at intermediate depths. The inflation event observed in 2008 was estimated to be the result of an injection of magma of ~0.08 km^3 that was followed in 2014 by an additional increase in volume of ~0.06 km^3. No periods of deflation were observed in the GPS data after these events, and we believe the total volume of magma accumulated in this region, ~0.2 km^3, remains in a shallow storage system beneath Akutan Volcano.

Published by Elsevier B.V.

1. Introduction

Akutan island is located in the central section of the 2000 km Aleutian volcanic arc, a product of the subduction of the Pacific plate beneath the Bering plate in the west and the North American plate in the east. The island is situated just west of the break in the continental shelf, so that the overriding crust in this region is transitional between continental and oceanic, with a thickness of 33–39 km (Janiszewski et al., 2013), and water depths surrounding the island are <100 m (Amante and Eakins, 2009) (Fig. 1, inset). The most prominent feature on Akutan island is the 1300 m composite stratovolcano of the same name (Fig. 1). The summit of Akutan volcano hosts a caldera that was formed 5.2 ka with a 1 km wide and 240 m high active cinder cone situated in the northeast quadrant of the caldera (Newhall and Dzurisin, 1988; Miller et al., 1998). Sulfur deposits can be found lining small craters within the caldera and active fumaroles are present along the southern flank. The only village on the island, Akutan village, has been established south of Hot Springs Bay, 13 km northeast of the volcano (Fig.1), where geothermal activity is used to provide power to the approximately 1000 inhabitants. To the east, the topography becomes a more complicated series of north-south trending ridges and valleys extending across the island, primarily composed of older, early Pleistocene ash and tephra deposits formed 1.5 to 3.3 Ma (Romick et al., 1990; McConnell et al., 1997; Miller et al., 1998; Richter et al., 1998).

Akutan is one of the most active volcanoes in the Aleutian arc (Lu and Dzurisin, 2014), with at least 27 eruptive events noted since 1790 (Finch, 1935; Byers and Barth, 1953; Simkin and Siebert, 1994; Miller et al., 1998), and it has been included in the top 10% of volcanoes that pose a risk to both life and property in the United States (Ewert, 2007). The most recent eruption, from March to May of 1992, consisted of repeated ash plumes and steam events (VEI 1) (McGimsey and Neal, 1996; Miller et al., 1998; Richter et al., 1998). Such explosive activity was reported on a 1–4 year cycle between the mid-1970s and early 1990s, while effusive eruptions are historically less common. When effusive eruptions do occur, lava flows are channeled from the summit of Akutan north, towards Long Valley, through a breach of the caldera rim; the last occurred in 1978 when a porphyritic two-pyroxene basaltic

---

* Corresponding author.
E-mail address: kdegrandpre@smu.edu (K. DeGrandpre).

https://doi.org/10.1016/j.jvolgeores.2017.10.003
0377-0273/Published by Elsevier B.V.

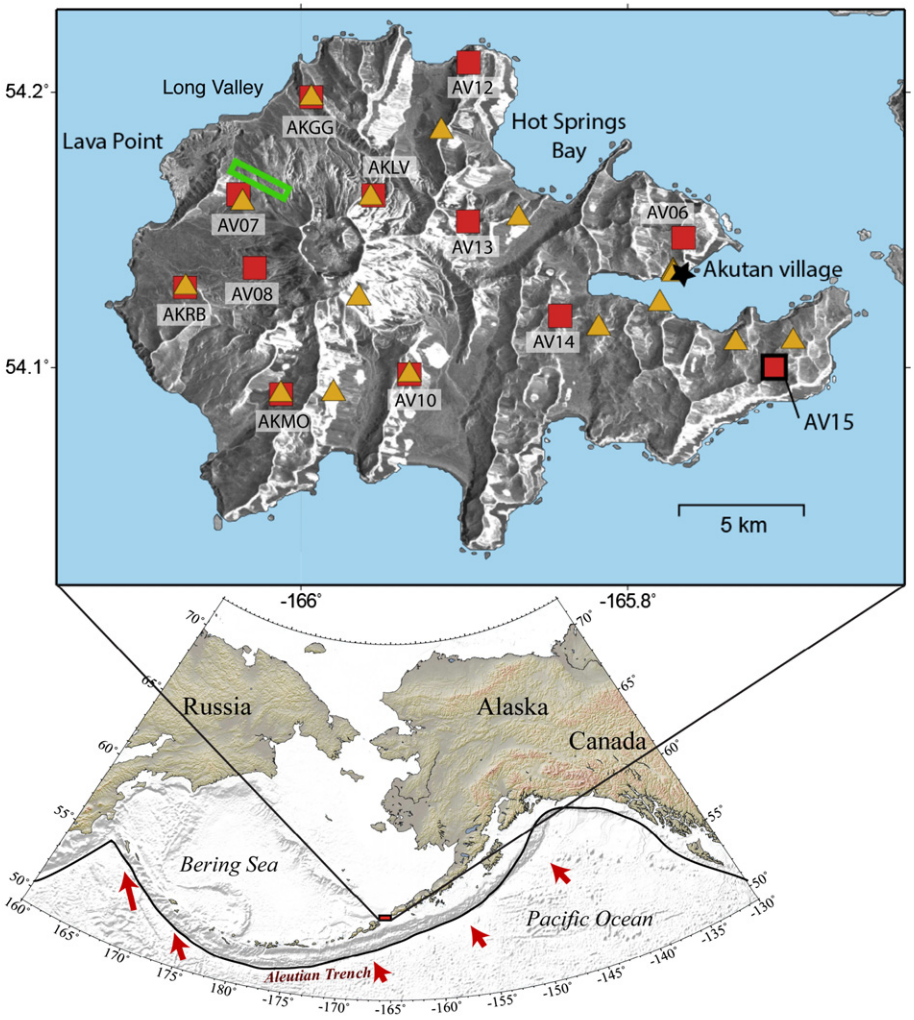

Fig. 1. Location map of Akutan island in the central section of the Aleutian arc. The break in the continental shelf can be seen in the bathymetry to the north of the highlighted area, and arrows indicate motion of the Pacific plate towards the Bering and North American plates along the Aleutian trench. The inset shows Akutan island, with Akutan village, Hot Springs Bay, and Lava Point labeled. GPS stations are plotted as red squares and seismic stations as yellow triangles, the stable reference GPS site, AV15, is labeled and located at the red square with the thick black border. The green rectangle outlines the approximate area of surficial ground cracks and extensional features that formed during the March 1996 earthquake swarm.

andesite erupted from the summit with simultaneous ejection of incandescent bombs. These bombs were witnessed by airline pilots to reach heights of 100 m above the summit and have subsequently been found distributed across the entirety of the island (Miller et al., 1998; Richter et al., 1998; Waythomas, 1999).

The tectonic and volcanic nature of Akutan island has led to seismic events both independent of and associated with eruptive events. These events were recorded only through historical accounts until March 1996, when instrumentation was installed following an intense period of seismic activity. With the onset of seismic activity, the Alaska Volcano Observatory (AVO) initially installed five seismometers, one in Akutan village and four on the eastern side of the island (Fig. 1). This network was augmented throughout the summer of 1996, when six additional permanent seismic stations were installed island-wide, and this number has since been increased to a total of 15 stations (Fig. 1). Using real-time, short-period, and broadband seismometers, over 3000 local seismic events have been located during this seismic swarm, with a peak in frequency observed between March 11 and 16, 1996 (Lu et al., 2000). No eruption resulted from this increase in activity, yet the 1996 seismic swarm was estimated to have released energy approximately equivalent to one magnitude 6 event (Power et al., 1996; Lu et al., 2000). There was, however, observed surface deformation associated with this event. During field work in July 1996 a series of fresh ground cracks were observed to discontinuously extend from Lava Point on the western coast along a strike of N250°E to the southeast side of the island. The most severely affected area was a 300–500 m wide rectangular zone between Lava Point and the western rim of the caldera (Waythomas, 1999) (Fig. 1).

Previous studies have used both Synthetic Aperture Radar Interferometry (InSAR) and GPS data to study the surface deformation related to volcanic processes at Akutan (Lu et al., 2000; Lu et al., 2005; Ji and Herring, 2011; Lu and Dzurisin, 2014). InSAR images were used to create interferograms that temporally span the duration of the 1996 seismic swarm and consistently exhibit uplift in excess of 60 cm over the western part of the island, with similar magnitudes of subsidence across the eastern extent. To explain the complicated spatial pattern observed in these interferograms several multi-source models have been proposed (Lu et al., 2000; Lu and Dzurisin, 2014), but the main deformation source responsible for uplift in the western part of the island is modeled as a shallow (<1 km) dike system extending 5–6 km laterally and 2–4 km down dip (Lu et al., 2000, 2005). Deformation before and after the seismic swarm was also analyzed through interferograms that

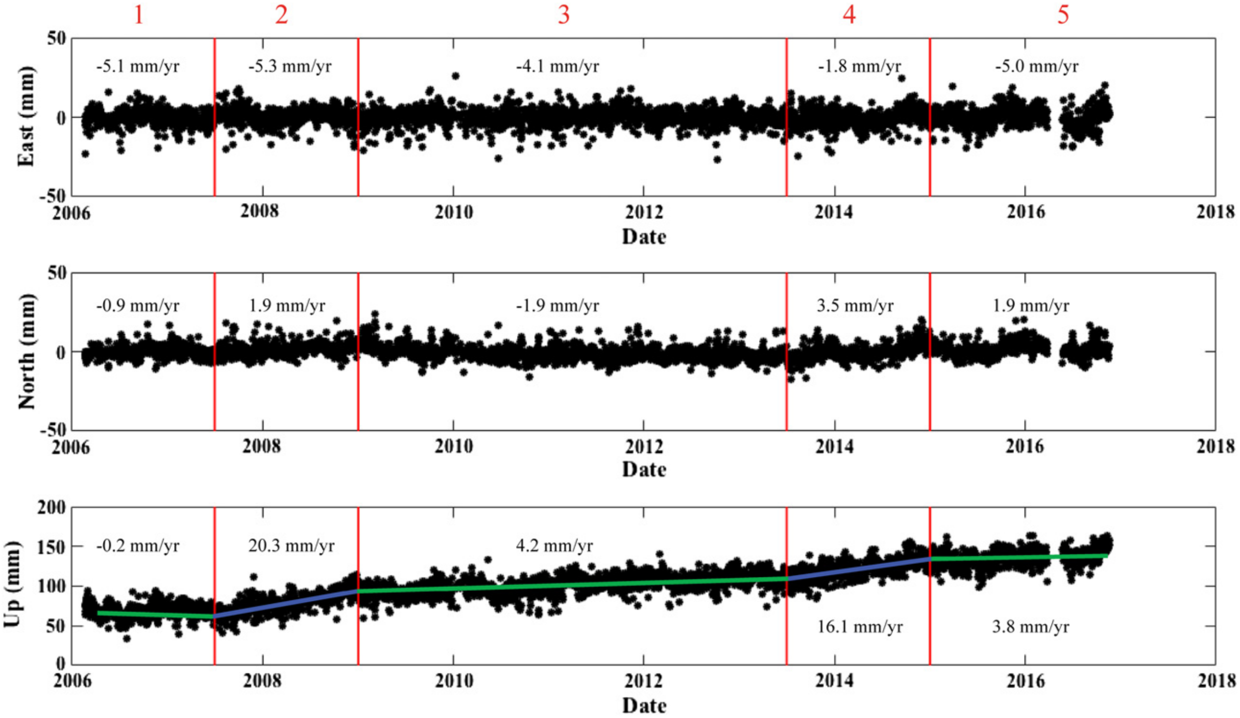

Fig. 2. Time-series of daily position solutions relative to stable North America with seasonal variations removed at GPS site AKLV are plotted for the east (top), north (middle) and vertical (bottom) components. The horizontal components, east and north, have been detrended, but deflation events are still barely visible. Red lines separate the five time periods, pre-2008 (1), 2008 event (2), 2009–2013 (3), 2014 event (4), and post-2014 (5). Additionally, all of the available data were used as a time period extending from the beginning of pre-2008 to the end of post-2014. Velocity estimates created using the model described in Section 3.1 are indicated for each time period, illustrating the sharp increase in velocity associated with the 2008 and 2014 inflation events.

show the volcano's northern flank uplifting ~10 mm per year (Lu et al., 2005; Lu and Dzurisin, 2014) and was explained by the intrusion of magma into a reservoir located 5–7 km beneath the northern flank of the volcano (Lu and Dzurisin, 2014). Interferograms created from images acquired after the swarm exhibit interesting additional deformation in the form of a linear subsidence pattern extending westward from the summit (Lu and Dzurisin, 2014). This subsidence coincides with the region mapped during field work in July 1996 that experienced the most extensive ground cracking. This onset of subsidence has been interpreted as the result of cooling and degassing of a magma intrusion that failed to erupt at the surface (Lu and Dzurisin, 2014). Additional persistent subsidence is observed inside the caldera, but is most likely related to the depressurization of a shallow hydrothermal system (Lu and Dzurisin, 2014).

While GPS data is limited spatially it can provide a very high resolution in time, with measurements at continuous stations being collected every 30 s. Using this high resolution temporal data, transient inflation during the first half of 2008 was detected and modeled by Ji and Herring (2011) as a simple Mogi source at shallow depth (~3.9 km).

A recent study reveals the complex nature of structures beneath Akutan island from the simultaneous inversion of the 1996–2009 seismic body and surface wave data for a more accurate velocity model and event relocations (Syracuse et al., 2015). The relocated earthquakes are clustered in four areas: 1) 8 km east of Akutan's caldera where most earthquakes occurred at very shallow depths during the 1996 swarm; 2) Northwest of the caldera, both onshore and offshore near Lava Point, indicating a northwest dipping plane located around 4–10 km depth; 3) A 6 km long vertical plane of seismicity beneath the north and northwest side of the caldera, with the same orientation of the observed ground cracks; 4) A region south of the caldera where most of the deep earthquakes (deeper than 10 km) occur (Syracuse et al., 2015).

The results of these previous studies suggest that the surface deformation may reflect multiple mechanisms both spatially and temporally. Here we divide continuous GPS data into five different time periods to better analyze the temporal evolution of deformation, from the time of the GPS site's installation (generally the summer of 2005, but as early as 2002), to the time of this study in November 2016. We then invert these data to produce a best estimate of the magmatic source geometry at Akutan volcano, and evaluate the evolution of its volume change with time. We also consider the cumulative deformation available at each GPS site for the whole ~10 year time series.

2. GPS data

There are 16 campaign and 12 continuous GPS sites installed on Akutan island (Fig. 1). GPS campaign sites are short term repeat occupations, and cannot provide the temporal resolution necessary to model the periods of episodic inflation. Thus, only data from the 12 continuous GPS sites are used in this study. These data are publically available through UNAVCO and the Plate Boundary Observatory (PBO; http://pbo.unavo.org). Daily position solutions were estimated for all data through the University of Alaska Fairbanks - Geophysical Institute using the GIPSY/OASIS II software goa-5.0 developed by the Jet Propulsion Laboratory in Pasadena, California following the processing

Table 1
Range of input parameters for Mogi model inversion. Longitude, latitude, and depth locations indicate the location of the point source at depth and volume is the change in volume required to produce the estimated surface deformation.

Bounds	Longitude (dec. deg. E)	Latitude (dec. deg. E)	Depth (km)	Volume (km^3)
Upper bound	−165.940	54.195	15.0	0.100
Lower bound	−166.000	54.090	0.0	−0.010

Table 2
Range of input parameters for Okada model inversion. Longitude, latitude, and depth locations indicate the center of the top edge of the dislocation plane. Length is measured as the top and bottom edges of the dislocation plane while width is measured in the down dip direction. The dip values are degrees from horizontal, and the direction of this angle is related to the strike direction in the conventional right-hand rule. Opening indicates the amount of dislocation of the defined geometric shape required to produce the surface deformation.

Bounds	Length (km)	Width (km)	Depth (km)	Dip (deg. from horz.)	Strike (deg. from N)	Longitude (dec. deg. E)	Latitude (dec. deg. N)	Opening (mm)
Upper bound	15	15	15.0	0	360.0	−165.940	54.195	5000
Lower bound	0.5	0.5	0.0	−90.0	0.0	−166.000	54.090	0

methods described by Fu et al., (2012). These GPS time-series (e.g. station AKLV, Fig. 2) exhibit two distinct pulses of rapid inflation on top of the steady rate of motion. In order to more accurately model the geophysical processes responsible for these episodic changes in velocity, the east, north, and up measurements were grouped into five time periods. The five periods are designed to isolate these episodic changes in velocity and to analyze the underlying constant rate of motion before, between, and after these inflation events. The two inflation events are defined from abrupt velocity changes in the vertical component. There are no published dates defining the 2014 event and published dates for the 2008 inflation event were determined by Ji and Herring (2011) using principal component analysis, and describe a six month event that took place in early 2008. These dates do not incorporate the obvious inflation that occurred in the end of 2007 and the beginning of 2009 that was a continuity of the 2008 inflation. The events defined in this study were done so from visual analysis of the vertical component of GPS site AKLV (Fig. 2). The first period, pre-2008 (Fig. 2 (1)), extends from the beginning of the available data (between 2002 and 2005) to July 1, 2007. The 2008 inflation episode, hereafter referred to as the 2008 event (Fig. 2 (2)) is defined from July 1, 2007 to Jan 1, 2009. The third period, 2009–2013 (Fig. 2 (3)), extends from Jan 1, 2009 to July 1, 2013, and July 1, 2013 to Jan 1, 2015 encompasses the second period of inflation (Fig. 2 (4)), referred to here as the 2014 event. The fifth period, post-2014 (Fig. 2(5)), covers all data available from Jan 1, 2015 to present (November 18, 2016). We also consider an additional data set based on all available data for each site, which has a variety of different time spans depending on the installation and functionality of each GPS site. The minimum required continuous set of data used to produce a deformation measurement was defined to be 1 year so that seasonal cycles do not dominate our velocity measurements. Because of this not every station has an estimation for every time frame, and some have shorter time durations for one period than the others (Tables S1–S7). These gaps in time-series data, seen in early 2016 at site AKLV (Fig. 2), are often a result from equipment malfunction or natural forces interrupting data transmission, and because of the remote nature of Akutan island, maintenance cannot always be performed in a timely manner.

3. Methods

The goal of this study is to observe the effect of volcanic processes at Akutan island, manifested as surface deformation during six time periods. In order to use the GPS data as accurately as possible, several processing steps were required. First, the measured daily position values were used to estimate velocity for each station during each time frame. To isolate volcanic displacement and remove dependency on a reference frame, a regional tectonic and reference frame velocity estimation is subtracted from the velocity estimate at each site for each time series. This volcanic rate was then converted into displacements for each time period and modeled using four source models. A buried point source (Mogi, 1958), a dislocation plane (Okada, 1985), a finite prolate or oblate spheroid (Yang et al., 1988), and a finite prolate or oblate ellipsoid (Yang et al., 1988) in a homogeneous isotropic elastic half space (hereafter refer to as Mogi, Okada, Yang-Spheroid, and Yang-Ellipsoid respectively), are compared in an effort to define source geometry and create a volume change time-series.

3.1. GPS velocity model

A velocity model relative to a stable North American plate (NOAM) (Eq. (1)) was first fit to daily solutions for each of the GPS sites, for each of the five time periods (Table S1). Gross outliers were stripped from the data and when data sets were long enough, cyclical seasonal terms were estimated and removed. When the data set was not long enough, seasonal terms were removed using model estimates based on satellite gravity data from the Gravity Recovery and Climate Experiment (GRACE) satellites (Fu and Freymueller, 2012), further details of the velocity model can be found in DeGrandpre (2015).

$$x(t) = a + bt + c_1 \sin(2\pi t) + c_2 \cos(2\pi t) + c_3 \sin(4\pi t) + c_4 \cos(4\pi t) \quad (1)$$

where a is position at time 0 (defined as the midpoint of the data), t is time, b is the slope, c_1–c_4 are seasonal coefficients. Not all of the terms included in Eq. (1) are required for every site, but the same terms are used for all three vector components. Daily positions are weighted based on the inverse of their covariance matrix.

3.2. GPS deformation

The velocities that were estimated using this model (Table S1), however, reflect the summation of all forces acting on a location. To isolate volcanic motion from the effects related to regional tectonics and use of the reference frame a velocity estimate for these values will be subtracted. There is no published model that provides this estimation, so in an effort to be as accurate as possible we make the assumption that the GPS site AV15, located on the far-east peninsula of Akutan

Table 3
Range of input parameters for Yang-Spheroid and Yang-Ellipsoid model inversions. Longitude, latitude, and depth locations indicate the center of the spheroid/ellipsoid. Length A and length B are the total distance of each respective axis, and the third, C axis, is equal to the B axis in the case of a spheroid, and is calculated using Eq. (2) in the case of the ellipsoid. The plunge values are degrees from horizontal, and the direction of this angle is related to the strike direction in the conventional right-hand rule. Pressure indicates the change in pressure of the defined geometric shape required to produce the surface deformation.

Bounds	Longitude (dec. deg. E)	Latitude (dec. deg. N)	Depth (km)	Pressure (kPa)	Length of A axis (km)	Length of B axis (km)	Strike (deg. from N)	Plunge (deg. from horz.)
Upper bound	−165.940	54.145	15.0	100,000.0	15.0	15.0	360.0	0.0
Lower bound	−166.000	54.090	0.0	5.0	0.5	0.5	0.0	−90.0

Table 4
Best fit model results for Akutan GPS data. Data is segmented into five different groups, with "All" encompassing all five data sets together. All data sets were best fit using the Yang-Spheroid model with the exception of the all and pre-2008 data, which are best fit using a Yang-Ellipsoid model. Estimated values have the same geometric relationship as previously described in Table 3. These are the resulting best fit parameters for each model. From the strike direction we determine the all and post-2014 data sets dip to the north and the pre-2008, 2008, 2009–2013, 2014 data sets dip to the south. Volume is calculated using this estimated pressure and lengths of the A, B, and C axes defined in Eq. (4). The WRSS is presented for each model, the statistical significance of these values is analyzed with Eq. (5) in Appendix B.

Data	Longitude (dec. deg. E)	Latitude (dec. deg. N)	Depth (km)	Pressure (kPa)	Length of A axis (km)	Length of B axis (km)	Strike (deg. from N)	Plunge (deg. from horz.)	Volume (km^3)	WRSS
All	−165.964	54.156	8.3	61,012.1	4.2	0.5	292	−63	1.7	808.5
Pre 2008	−166.000	54.130	9.1	18.2	5.2	12.9	105	−33	0.05	7.3
2008	−165.953	54.151	7.7	40,086.7	1.3	3.4	165	−64	0.08	1.1
2009–2013	−165.966	54.155	8.6	348.7	4.9	4.3	137	−58	0.01	12.2
2014	−165.965	54.148	7.6	5910	2.8	2.4	150	−64	0.03	1.3
Post 2014	−165.949	54.149	9.3	1656.4	3.0	8.8	283	−62	0.04	1.8

island (Fig. 1) reflects motion related to only tectonic forces and reference frame calculations for the horizontal components. The assumption that AV15 is far enough from the magma source and therefore is not affected by volcanic deformation is based on previous studies that show little localized deformation in this area (e.g., Ji and Herring, 2011; Lu and Dzurisin, 2014). To ensure that the removal of the horizontal components of AV15 is the best tectonic estimate available, five other methods for estimating the tectonic motion were also removed from the data and compared for all four models (Appendix A). The east and north velocities at AV15 for each time period were subtracted from the east and north velocities at each of the GPS sites (AV15 included) for the same time period. The tectonic contribution to the vertical displacement is assumed to be minimal compared to the volcanic influence and no adjustment is made to the observed data. All components (east, north, and vertical) were then multiplied by the total time for that particular period. When the length of time is not defined by the period and GPS sites have variable durations of observation (all, pre-2008, and post-2014), the time used to calculate displacement is taken from the GPS site with the least amount of time (Tables S2, S6, and S7). For the periods with temporal bounds restricting the data (2008 event, 2009–2013, and 2014 event) the defined duration of each period (1.5, 4.5, and 1.5 years, respectively), was used to calculate displacement (Tables S3–S5). These resulting values that have been corrected for an estimated horizontal tectonic influence are hereafter referred to as calculated volcanic displacements. This subtraction eliminates the reference frame and any tectonic signals, so that the resulting calculated displacement is assumed to be a direct result of volcanic effects.

$$d_{i,j} = (v_{i,j} - v_{AV15,j})^* \, t_j \tag{2}$$

where $d_{i,j}$ is the volcanic deformation at site i during time period j, $v_{i,j}$ and $t_{i,j}$ are velocity estimated from the model described in Eq. (1) and time span of data used to calculate that velocity at site i during time period j, and $v_{AV15,j}$ is the velocity estimation for site AV15 during the j^{th} time period. This equation is only applied to the east and north components.

3.3. Models

We estimated displacements during each of the five time periods using both Mogi (Mogi, 1958), Okada (Okada, 1985), Yang-Spheroid (Yang et al., 1988), and Yang-Ellipsoid models. The east, north, and vertical deformation at all 12 of the GPS site locations (dependent on data availability) were estimated by these models through a non-linear least squares inversion of 1000 Monte Carlo simulations using the "trust-region-reflective" optimization algorithm to minimize the weighted residual sum of squares (WRSS) with an error tolerance of 0.0001, which results in a prediction of model parameters that best fit the data. The residual for each component of motion was weighted by the inverse of the variance for each measurement at a particular site during the time period being modeled (Tables S2–S7). Poisson's ratio is fixed to 0.25 for all models and the first and second Lamé parameters used in the Yang-Spheroid and Yang-Ellipsoid models are both defined as 1 GPa. Topographic corrections were not made, so that depths are expressed as below sea level, and not necessarily ground surface. Because the datasets are relatively small (maximum number of data points is 36) and numerous simulations (1000) could be run with reasonable efficiency the input range for all parameters was quite high in all of the models (Tables 1–4). The large number of simulations also makes refining parameters and progressively fixing them with additional model runs unnecessary, as is often done in similar studies using deformation modeling approaches (Lu et al., 2000), because the first hundred best fit models would converge on similar parameter values.

The Mogi model uses four parameters to define a source that produces surface deformation: x, y, z location (longitude, latitude, and depth) and volume change (Mogi, 1958). The x, y, and z parameters indicate the center of a spherical point source at depth, with radial expansion of this point source resulting from positive volume changes, indicating inflation, and expressed on the surface as uplift, while negative volume changes are characterized by subsidence (Mogi, 1958).

The Okada model utilizes ten parameters. The source geometry makes up seven of the parameters, x, y, z location (longitude, latitude, and depth), strike direction, dip angle, length, and width, and the last three parameters characterize three-dimensional motion of the dislocation plane as dip-slip, strike-slip, and opening (Okada, 1985). Volume change for a dike or sill can be estimated from this model by multiplying the length, width, and opening values. The x, y, and z location is defined in this study as center of the top of the dislocation plane. Dip values are expressed in degrees from horizontal, following the American right hand conventional relationship to strike (expressed in degrees from north), so that a strike of N90°E is dipping to the south and a strike of N270°E dips to the north. Two sets of upper and lower boundary inputs were used for the Okada modeling to aid in efficiency. The first set used a range of strike angles that are associated with south dipping planes, and the second was a range of strike directions that are related to north dipping planes. Each set was run as an independent model described above with 1000 Monte Carlo simulations. Because the focus of this study is on volcanic deformation and tectonic contributions have been removed, the dip-slip and strike-slip parameters were fixed to zero for all of the Okada models presented. Smaller, localized faulting most likely occurs in this dynamic volcano-tectonic environment, but with a lack of surface expressions or direct evidence of sudden offsets in the GPS data we assume that this effect is minimal compared to effects from changes to the volume of magma being stored. This results in the assumption that the observed relative deformation is directly related to an opening dislocation, requiring

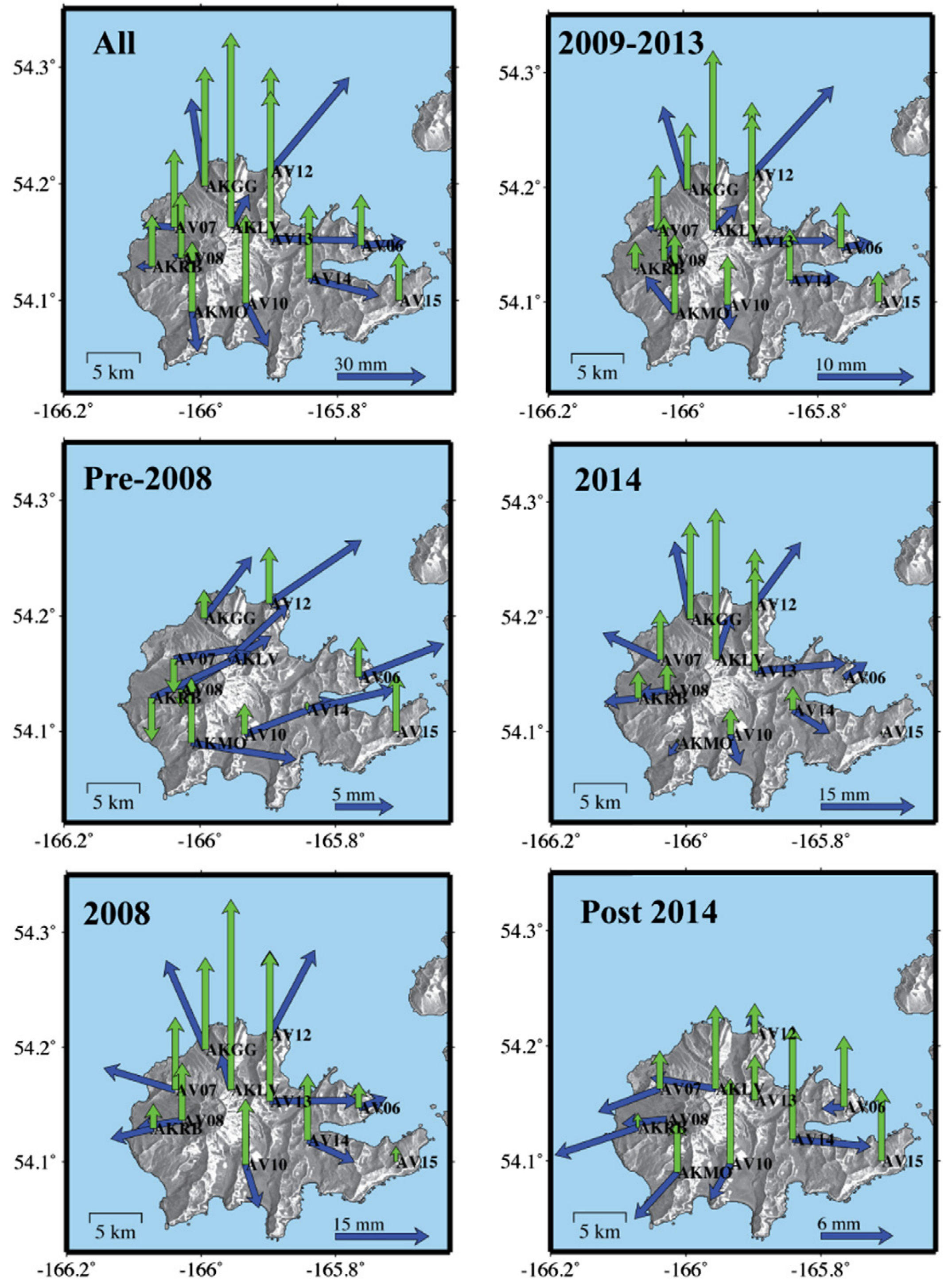

Fig. 3. Calculated volcanic displacement at 12 GPS sites for six different time periods. An estimation of tectonic velocity and reference frame contribution have been removed from the raw horizontal data. Blue arrows are total horizontal displacements and green arrows are total vertical displacements for each time period. Scale applies to both vertical and horizontal displacements. Note the occasional change in scale.

magmatic volume changes along a dipping plane to produce surface displacement. This reduces the degrees of freedom (DOF) in our Okada models to eight parameters.

The Yang-Spheroid model also requires the input of eight parameters (Yang et al., 1988). The source is defined by the x, y, z location (longitude, latitude, and depth) of the center of the spheroid, strike of the B axis, dip angle of the A axis, length of the A axis, length of the B axis, and the pressure change required to produce the observed surface deformation. The Yang-Spheroid model is defined as a prolate or oblate spheroid, depending on the relationship between the A and B axes. Our models created a prolate spheroid when the A axis is longer than the B axis and an oblate spheroid when the opposite is true. The C axis is defined in the model as equal to the smaller axis to create a true spheroid (Yang et al., 1988).

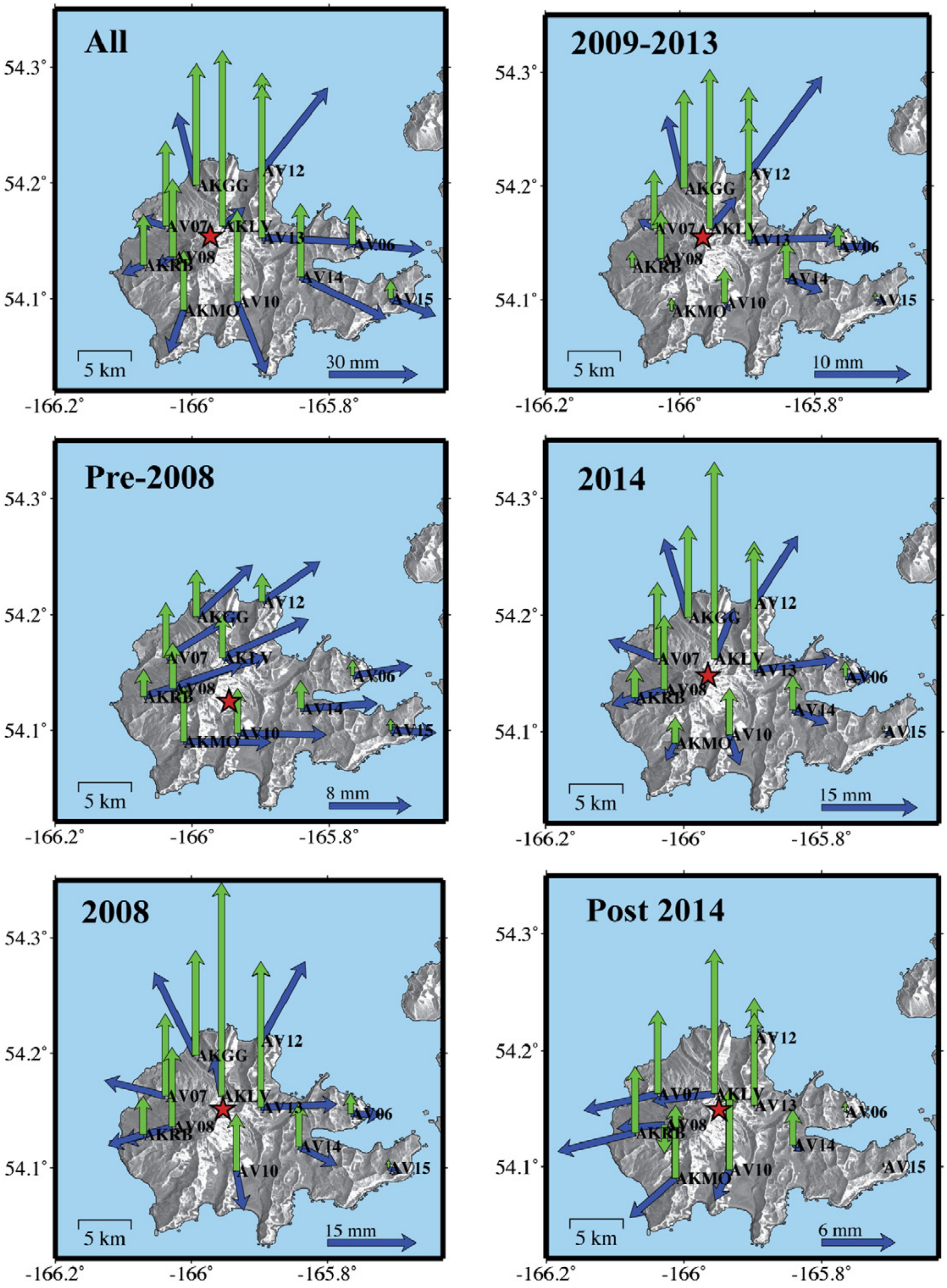

Fig. 4. Displacement estimates resulting from the best fit Yang-Spheroid models for five different periods of GPS data at Akutan Island. The all and pre-2008 data is best fit by a Yang-Ellipsoid model and the results are shown here. Blue arrows are total horizontal displacements and green arrows are total vertical displacements for each time frame. Red stars indicate the location of the center of the spheroid or ellipsoid. Note the occasional change in scale.

The Yang-Ellipsoid model is defined in exactly the same way as the Yang-Spheroid model with the only exception being the calculation of the C axis. In the Yang-Ellipsoid model the C axis is calculated using Eq. (3).

$$c = \sqrt{a^2 - b^2} \tag{3}$$

where a, b, and c are the axis lengths defining an ellipsoid.

Volume change for the Yang-Spheroid and Yang-Ellipsoid models was calculated using Eq. (4), following methods used at Long Valley Caldera (Tiampo et al., 2000; Battaglia et al., 2003; Newman et al., 2006) and Campi Flegrei (Battaglia et al., 2006). This volume estimation is most accurately used for ellipsoids that are nearly spheres (Amoruso and Crescentini, 2009) and is actually representative of the volume change relative to the mechanical properties of the surrounding half-space and not the injection volume of a compressible fluid (Dzurisin,

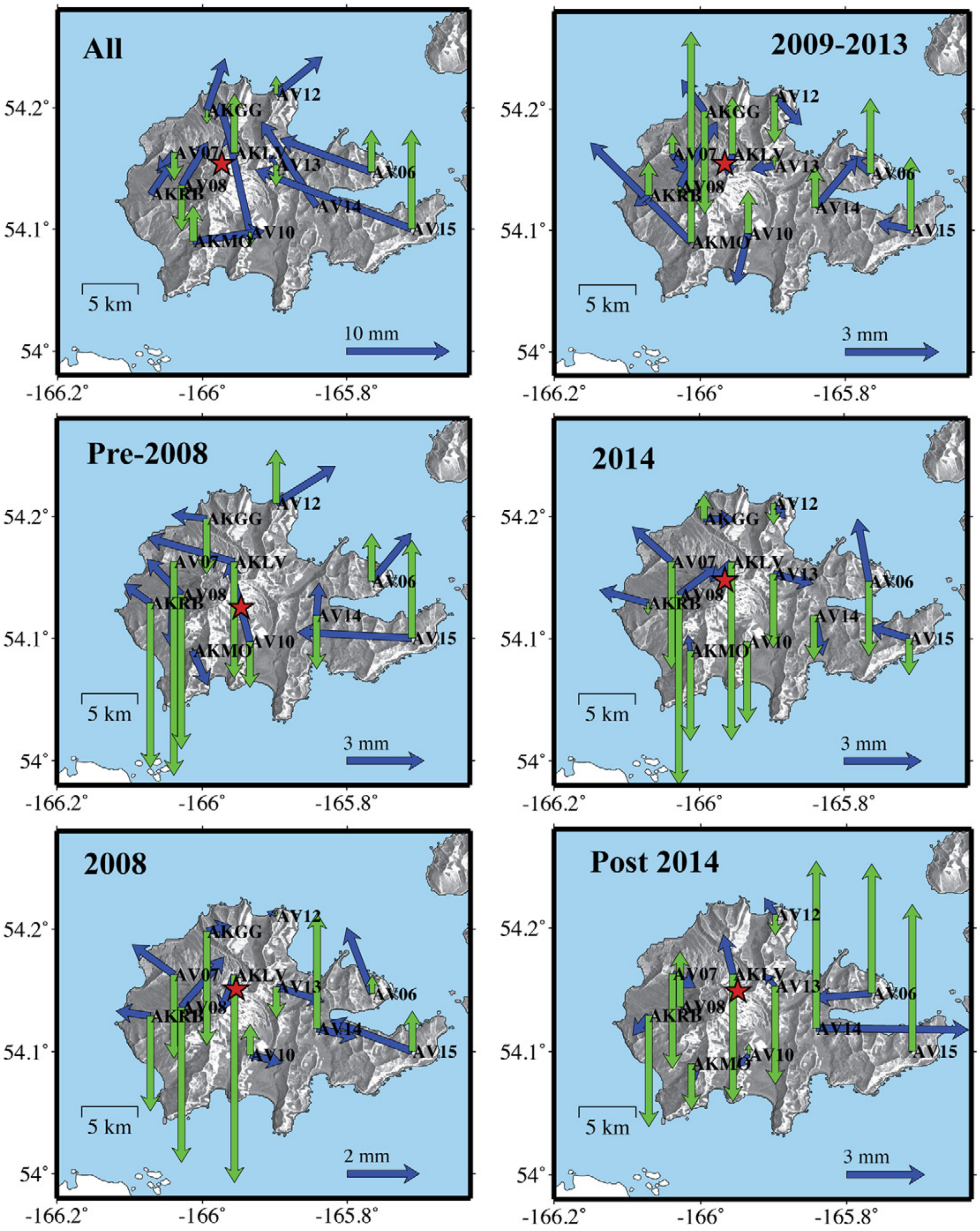
All

2009-2013

Pre-2008

2014

2008

Post 2014

Fig. 5. Residuals between calculated volcanic deformation data and model estimates for six different periods of GPS data at Akutan Island. Blue arrows are total horizontal displacements and green arrows are total vertical displacements for each time frame. Red stars indicate the location of the center of the spheroid or ellipsoid. Note the occasional change in scale.

2006). However, with little information on the compressibility and physical parameters defining the magma (Rivalta and Segall, 2008) at Akutan volcano we consider this volume estimation to be adequate for the purposes of this study.

$$\Delta V = \frac{\Delta P \pi}{\mu} abc \tag{4}$$

where ΔV is volume change, ΔP is pressure change, a, b, and c are the lengths of the A, B, and C axes, respectively, and μ is the second Lamé parameter (shear modulus). ΔP, a, b, and c are estimated from the Yang-Spheroid and Yang-Ellipsoid models, while μ was fixed to 1 GPa for all models (Davis et al., 1974; Rubin and Pollard, 1988; Bonaccorso, 1996; Dzurisin, 2006).

4. Results

4.1. Volcanic deformation

Spatial maps of calculated volcanic displacements for all time periods are shown in Fig. 3, and capture the complicated temporal evolution of surficial deformation at Akutan. The two periods of inflation

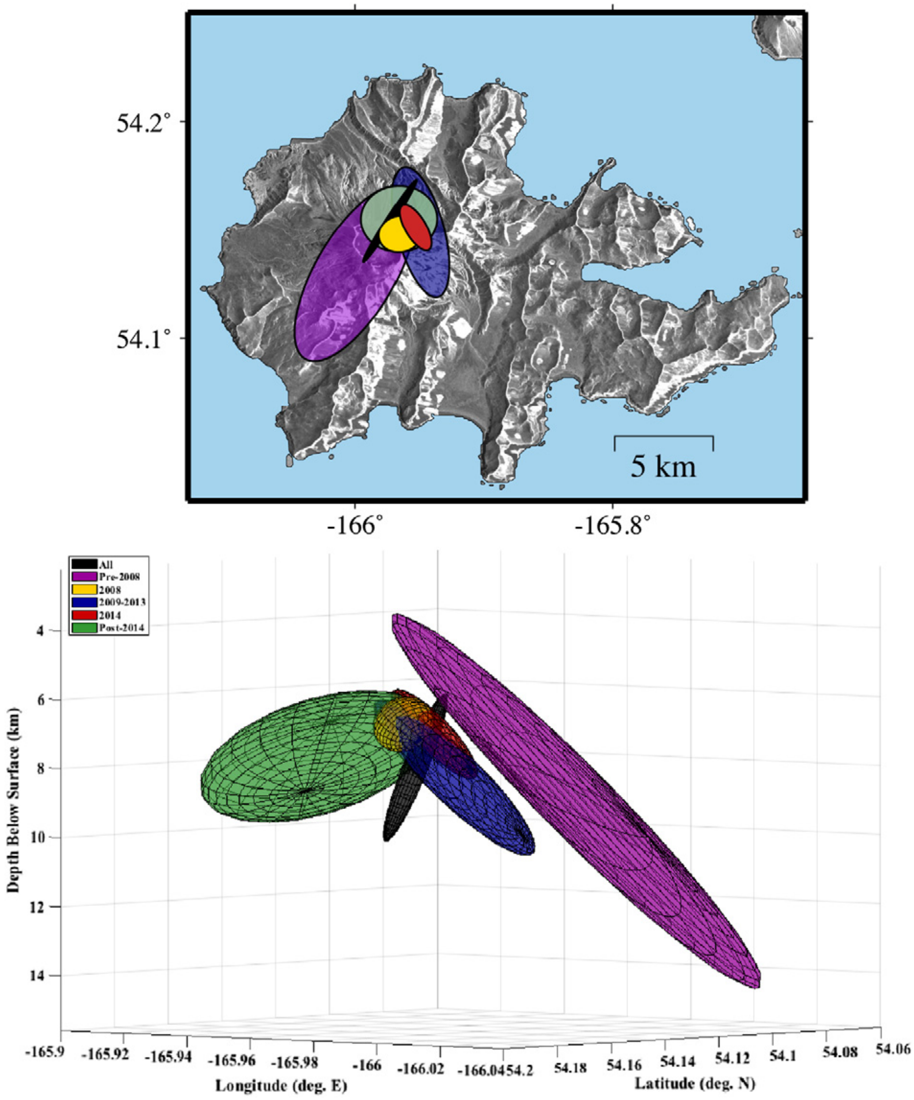

Fig. 6. Source locations for each of the best fit models in each time period in map view (top) and in three dimensions looking from northwest to southeast (bottom). All is in black, pre-2008 is purple, 2008 is yellow, 2009–2013 is blue, 2014 is red, and post-2014 is green. The model parameters can be found in Table 1.

(2008 and 2014) (Fig. 3 and Tables S3 and S5) are apparently significant when compared to the deformation pre-2008, 2009–2013, and post-2014 (Fig. 3 and Tables S2, S4, and S6) and dominate the overall signal (Fig. 3 and Table S7). The deformation for these 2008 and 2014 events reveal similar magnitudes of both horizontal and vertical deformation and radial horizontal spatial patterns around the summit of Akutan, with maximum uplift on the north flank of the volcano. The similarities between the two events suggests that the mechanism responsible for this deformation is likely the same and the same source has undergone multiple episodes of magma injection.

The pre-2008 data (Fig. 3) has strong horizontal motions to the east, with subsidence on the west flank of the volcano and uplift everywhere else. Subsidence is indicative of cooling or contraction of a magma source and occurs in the region of the observed 1996 ground cracks. The 2009–2013 deformation (Fig. 3) on the southern and western flanks of the volcano is small and randomized. The north side of the island, however, retains similar magnitudes and directions in both the vertical and horizontal motion as seen in the inflation events, potentially indicating that there is either a constant source on the north side of the island, or additional shallow processes related to geothermal energy could be contributing to a more localized signal. Deformation after the 2014 event (Fig. 3) appears to have systematic uplift island wide and southwestward motion isolated on the southwest flank of the volcano with little to no signal across the rest of the volcano.

Table 5
Range of input parameters for the restricted input Yang-Spheroid model. Description of model parameters can be found in Table 3.

Data	Longitude (dec. deg. E)	Latitude (dec. deg. N)	Depth (km)	Pressure (kPa)	Length of A axis (km)	Length of B axis (km)	Strike (deg. from N)	Plunge (deg. from horz.)
Upper bound	−165.952	54.152	8.0	100,000.0	1.5	3.6	190.0	70.0
Lower bound	−165.957	54.147	7.3	0.0	1.0	3.0	160.0	60.0

Table 6
Model results from the best fit Yang-Spheroid model, when the initial parameters were restricted to the 2008/2014 best fit models (Table 4). Estimated values have the same geometric relationship as previously described in Table 3.

Data	Longitude (dec. deg. E)	Latitude (dec. deg. N)	Depth (km)	Pressure (kPa)	Length of A axis (km)	Length of B axis (km)	Strike (deg. from N)	Plunge (deg. from horz.)	Volume (km^3)	WRSS
All	−165.952	54.151	8.0	10,334.6	1.3	3.1	160.0	60.0	0.2	14,447.0
Pre 2008	−165.952	54.147	7.3	2.7	1.0	3.6	160.0	60.0	0.00003	59.1
2008	−165.953	54.151	7.7	4041.8	1.3	3.3	165.2	63.7	0.08	1.1
2009–2013	−165.957	54.152	8.0	2666.2	1.2	3.6	160.0	60.0	0.04	24.4
2014	−165.957	54.148	7.3	4745.7	1.1	3.0	160.0	64.5	0.06	1.8
Post 2014	−165.952	54.150	8.0	1104.7	1.5	3.0	190.0	70.0	0.02	6.0

4.2. Statistical significance between models

WRSS values are calculated from the inversion of the calculated volcanic deformation for each of the four models (Appendix B). However, since the models have different DOF, these WRSS values cannot be directly compared. The Okada, Yang-Spheroid, and Yang-Ellipsoid models, have eight parameters, as opposed to the four parameters in the Mogi model, so it is expected that the best fit would come from the model with more DOF. In order to assess which model is statistically significant, an experimental F-test was calculated (Eq. (5)) between the Okada, Yang-Spheroid, and Yang-Ellipsoid WRSS values with the Mogi model WRSS during each time period (Appendix B) following methods described by Dzurisin et al. (2009).

$$F_{calc} = \frac{(WRSS_1 - WRSS_2)/(p_1 - p_2)}{WRSS_2/(N - p_2)} \tag{5}$$

where $WRSS$ is the weighted residual sum of squares for model 1 and model 2, p is the number of model parameters, and N is the number of data, in this case either 36 or 33 depending on the data set (Appendix B).

If the F_{calc} value is greater than the critical value for the Fisher-Snedecor F distribution, with a desired rejection probability of alpha, where F_{crit} is defined as $F_{p2-p1,\ N-p2,\ \alpha}$, then the smaller WRSS obtained with a more complex model is statistically significant (Dzurisin et al., 2009). F_{crit} for alpha values of 0.05 and 0.01 (95% and 99% confidence) are presented in Table 2, and show that with 99% confidence we can say for all time periods, except for all and pre-2008, the Yang-Spheroid model is the best fit. The Yang-Ellipsoid remains the statistically best fit model for the all and pre-2008 time periods.

4.3. Best fit models

For all of the time periods the Yang-Spheroid proves to be the statistically significant best fit, with the exception of the all and pre-2008 data, where the Yang-Ellipsoid fits best (Appendix B and Table 4). For all time periods the best fit models locate the center of the ellipsoid just northeast of the caldera rim at depths of 7.5 to 9.3 km below sea level, though the pre-2008 model is shifted to the southeast. The lengths of the axes of the ellipsoid and change in pressure vary from 0.5–13 km and 18–61,012 kPa, respectively. The 2008 event, 2009–2013, and the 2014 event are all striking to the southeast, therefore dipping to the southwest. The all, pre-2008, and post-2014 time periods are oppositely characterized as striking to the northwest and dipping to the northeast. All of the models have fairly steep dips of 60°–70° below horizontal, except for the pre-2008 Yang-Ellipsoid model that has a shallow dip of ~30° (Table 4). Another inconsistency between models is the general shapes. The 2009–2013 and 2014 events are almost spherical, the 2008 event and post-2014 data are fit by an oblate spheroid, and pre-2008 and all data sets are prolate.

The model predictions (Fig. 4) show similar patterns and magnitudes to the calculated volcanic deformation (Fig. 3). This is even more evident when the residuals are considered (Fig. 5). The horizontal residuals are noticeably small and randomized, while the vertical residuals are larger and often systematic near the volcano, but get smaller and more randomized moving east across the island. When the sources are compared in a depth profile and map view (Fig. 6) the similarities become clearer and the geometric consistency with which the 2008 event, 2009–2013, and 2014 events occur highlights the validity of these inflation events, while the all, pre-2008, and post-2014 data sets are fit by different models with unrealistic parameters. While the larger deformation events are fit by compact source models of similar shapes and sizes, the time periods with a very small signal (pre-2008 and post-2014) are fit by very large models with small changes in pressure. The all, pre-2008, and post-2014 data show that the depth, volume, and pressure change are not stable in the inversion when the deformation is either a large averaged signal (all), or very small signal (pre-2008 and post-2014). Isolating these parameters when the dataset is averaged or very small, would require better definition of the physical constraints regarding the source depth, volume, or pressure change.

4.4. Restricted input Yang-Spheroid models

The pre-2008, and post-2014 data sets all have relatively small displacements, which make them more difficult to model in general. To test whether the best fit parameters for these models were realistic, or if there was a constant spheroid geometry and orientation that is just undergoing episodic injection, these data sets were inverted again using a restricted range for upper and lower input boundaries. Because the 2008 event had the largest associated deformation and the 2014 event was geometrically similar with changes only in amount of volume injected, these parameters were used as a basis for the new model (Table 5). We are interested in exploring the change in magma volume with time, so the longitude, latitude, depth, axes lengths, strike, and plunge angles, were restricted to the range of the 2008 and 2014 events, so that the pressure change (and thus volume change) could vary with time, allowing for magma flux in four dimensions, while fixing the general location and orientation of one constant source mechanism.

A restricted input Yang-Spheroid model was created with upper and lower parameter boundaries of ~1–3.6 km for length of the axes, 7.3–8 km for depth, 60°–70° from horizontal dip angle, N160° E–N190° E strike direction (implying all dips are to the south), −165.957° E to −165.952° E longitude, 54.147° N–54.152° N latitude, and pressure change was left open at 0–100000 kPa. This modeling was run following the same procedures used for the original inversion of data described in Section 3.3.

Because the input parameter range (Table 5) is restricted, all of the models hold similar, oblate spheroid geometries and locations (Table 6). The all, 2009–2013, and post 2014 models are fit on the upper bound of depth at 8 km bsl, while the pre-2008 and 2014 event are on the lower depth boundary of 7.3 km bsl. The pressure changes, however, show an interesting progression, especially when calculated in terms of magma volume change, indicating the 2008 event was larger than the 2014 event. When the independently estimated volumes for

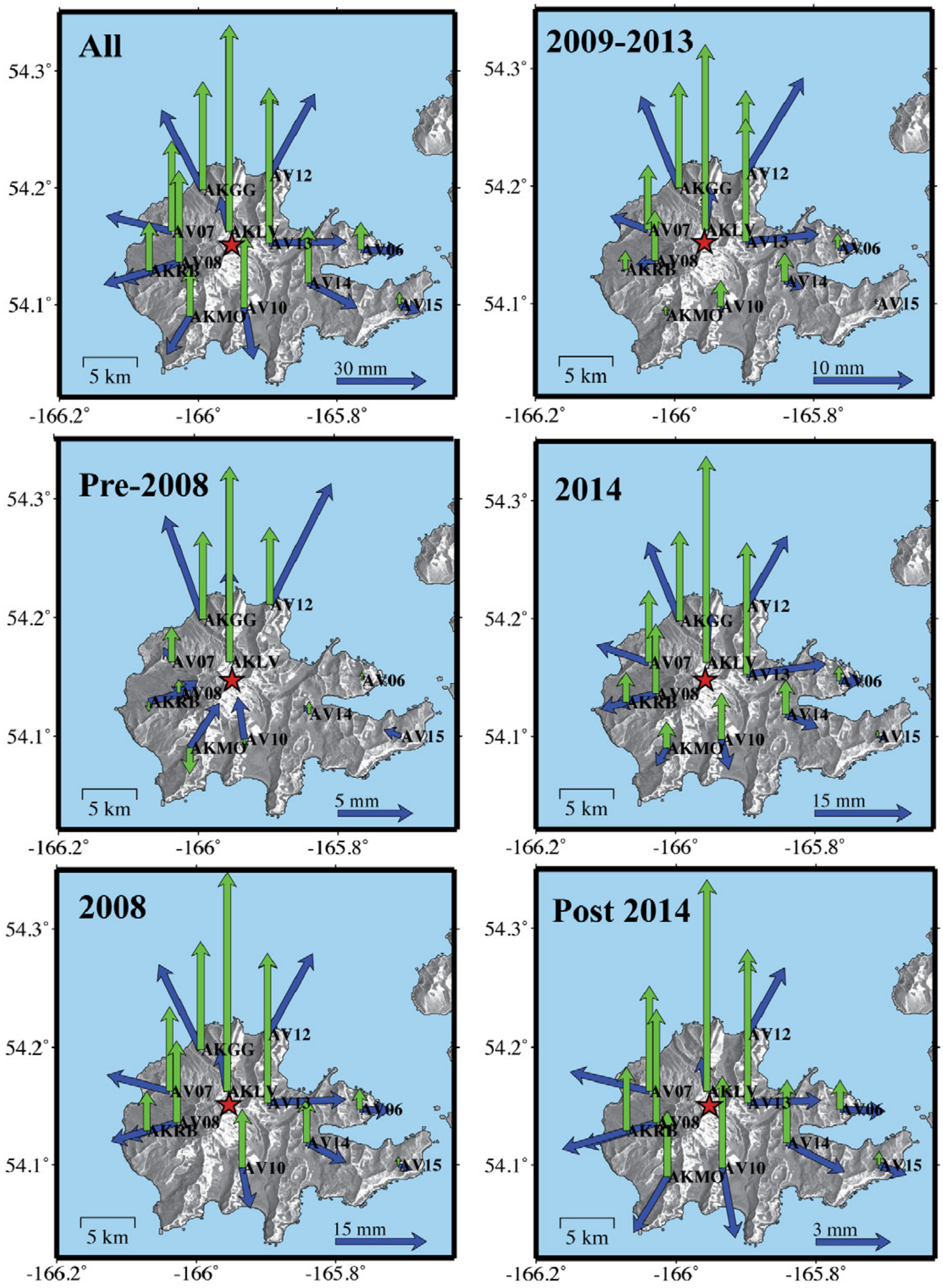

Fig. 7. Displacement estimates resulting from the restricted input Yang-Spheroid models for six different periods of GPS data at Akutan Island. Blue arrows are total horizontal displacements and green arrows are total vertical displacements for each time frame. Red stars indicate the location of the center of the Yang-Spheroid. Note the occasional change in scale.

each time period are summed, they are equal to the estimate of the all data set (0.2 km^3). While the models for the all, 2008, 2009–2013, and 2014 data sets all produce deformation magnitudes and spatial patterns (Fig. 7) similar to the best fit models (Fig. 4), the pre-2008 and post-2014 deformation is visually different, with more radial horizontal patterns and larger, asymmetric vertical deformation that is largest on the northern flank of the volcano in these restricted in put models (Fig. 7), rather than a constant, smaller vertical prediction island wide for both of the data sets best fit models (Fig. 4).

Logically, the residuals for these restricted input parameter models have a similar relationship with the best fit models as the predictions do. The residuals for the all, 2008, 2009–2013, and 2014 data all remain small and randomized (Fig. 8), like the best fit model residuals (Fig. 5). The pre-2008 residuals (Fig. 8), however are much larger and have a

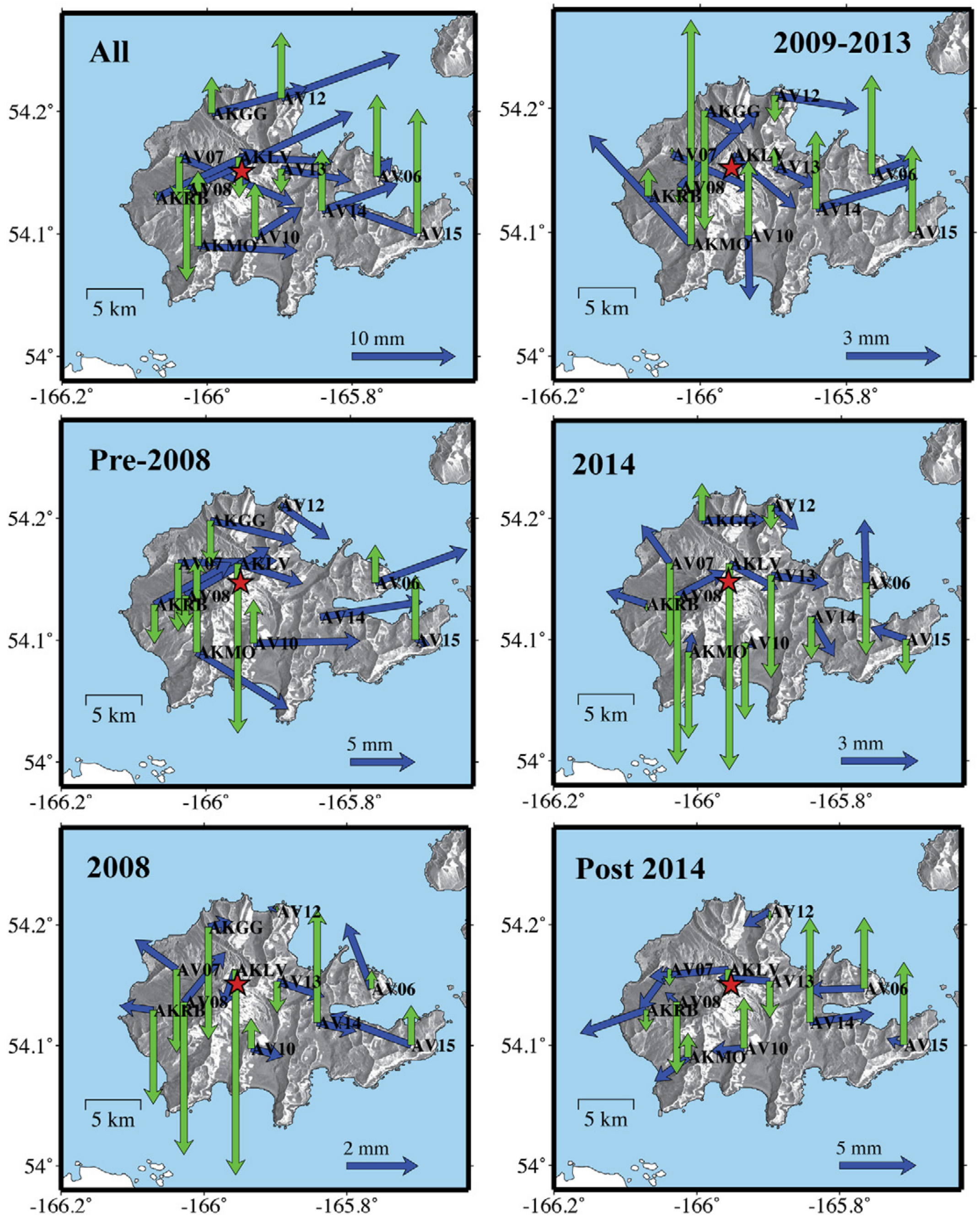

Fig. 8. Residuals between observed data and restricted input Yang-Spheroid model estimates for six different periods of GPS data at Akutan Island. Blue arrows are total horizontal displacements and green arrows are total vertical displacements for each time frame. Red stars indicate the location of the center of the Yang-Spheroid. Note the occasional change in scale.

spatial pattern that looks to be related to the tectonic estimate, in a systematic shift to the east. While the post-2014 residuals (Fig. 8) are still randomized, they are larger than the best fit model residuals (Fig. 5) by a few millimeters. The residuals for both of these time periods strongly resemble the calculated volcanic displacement (Fig. 3).

Comparison of the WRSS values for the original best fit models (Table 4) and these restricted input inversions (Table 6) shows that while these models are a worse fit to the all, pre-2008, 2009–2013, and post-2014 data sets, it is not a drastic change. The 2008 inflation event does not have an increased WRSS, as expected because the parameters are restricted according to the best model, and the 2014 event has only a minor increase in the WRSS.

5. Discussion

5.1. Interpretation of deformation at Akutan

From our analysis, it is clear that two inflation events occurred at Akutan in 2008 and 2014. These events are believed to be occurring at one consistent source located under the northern flank of the volcano, with the 2008 event resulting from a larger injection of magma (0.08 km^3) than the 2014 event (0.06 km^3). There is no deflation after the 2008 event, so we assume that this larger injection of magma is being stored at a depth 6–9 km bsl, and the 2014 event signifies an additional pulse of magma. With no eruption occurring in either event, and no deflation happening in the post-2014 time frame it appears that Akutan is capable of storing large amounts of magma (0.2 km^3), at intermediate depths (~6–10 km). The source appears to have a smaller, constant influx of magma during the time between these two events (2009–2013) because the magnitude of deformation and the associated volume change (0.04 km^3) during this time is smaller than either event, yet still considerable. The spatial inconsistency of the observations, lacking any sort of systematic gradational pattern expected to be associated with volcanic deformation infers that the physical reality of the estimated model parameters during this interim time is not significant. The parameters, however, remain somewhat consistent and the residuals are small and random for both the open input and restricted input Yang-Spheroid models during the two events and the time period between them (Figs. 5 and 8 and Tables 4 and 6). We consider these models to represent a realistic migration of magma to a shallow, oblate spheroidal, storage chamber on the northern flank of Akutan volcano, from the resulting parameters defined through inversion of the calculated volcanic deformation GPS data.

The data sets for the pre-2008 event and post-2014 event suggest that different processes occurred during those time periods. In the pre-2008 data we observe a small amount of subsidence on the western flank of the volcano, with larger uplift in the northern and eastern regions and general horizontal motion to the northeast islandwide (Fig. 3). This deformation is not easily modeled using the methods implemented here, but the small area of subsidence in the west is believed to be associated with the crystallization and cooling of the shallow intrusion that has resulted in the ground cracks mapped in 1996. The horizontal magnitude is large enough to model, but the motion and pattern is most likely related to our estimated tectonic motion, as it is almost equal and opposite to the motion subtracted. The post-2014 observations (Fig. 3) resemble radial Mogi deformation, except that there is no systematic gradient in the vertical magnitude, and the magnitude of the horizontal deformation increase away from the center.

The residuals for the best fit models during each of the time periods vary in magnitude, but remain randomized in the vertical and most noticeably in the horizontal. Because the horizontal residuals are generally quite small (<5 mm) they are not used in any additional modeling efforts, and the source interpretation is simply a one mechanism source.

The total data available for each site was modeled throughout this study, but as the complex temporal nature of the deformation of Akutan became clear, this data set became obsolete in our assessment of the change in source volume with time. The total data model results are clearly dominated by the 2008 and 2014 inflation events, but are also influenced by the trends surrounding those events and therefore do not accurately reflect the nature of the individual processes taking place at any particular time period. The volume for each of these data sets is calculated from the pressure change and axes lengths parameters and the change in pressure and change in volume cannot be linearly related. However, the magnitude of this overall data set did provide an additional check on the volume estimations, in that the estimated volume for this all data set (0.2 km^3) was equal to the sum of the individually calculated volumes for each time period.

5.2. Comparison of GPS deformation and seismic velocity inversions

Syracuse et al. (2015) present seismic relocations and tomography (Figs. 9 and 10) beneath Akutan volcano with additional interpretation based on their inversions and the geodetic work by Lu et al. (2000), Ji and Herring (2011), and Lu and Dzurisin (2014). The seismic relocations and tomography are the result of the simultaneous inversion of seismic events using the program TomoDD (Zhang and Thurber, 2003; Zhang and Thurber, 2006). The interpretation provided in their study involves a cracked and cooler vertical conduit through which episodic injections are transferred from the bottom of the crust to a storage system located at 7–10 km depth, causing associated deeper seismic swarms. This injected magma is then stored in the upper crust, below the center of the caldera, creating the observed aseismic zone of hot partially melted magma. Shallow regions beneath the caldera are interpreted to represent highly fractured vertical diking systems created when failed eruptions cooled at shallow depths of around 4 km, which they relate to the deformation modeled by Ji and Herring (2011). Their interpretation is slightly deeper than the main location of magma accumulation proposed by Lu and Dzurisin (2014) of 5–7 km depth, but the presence in

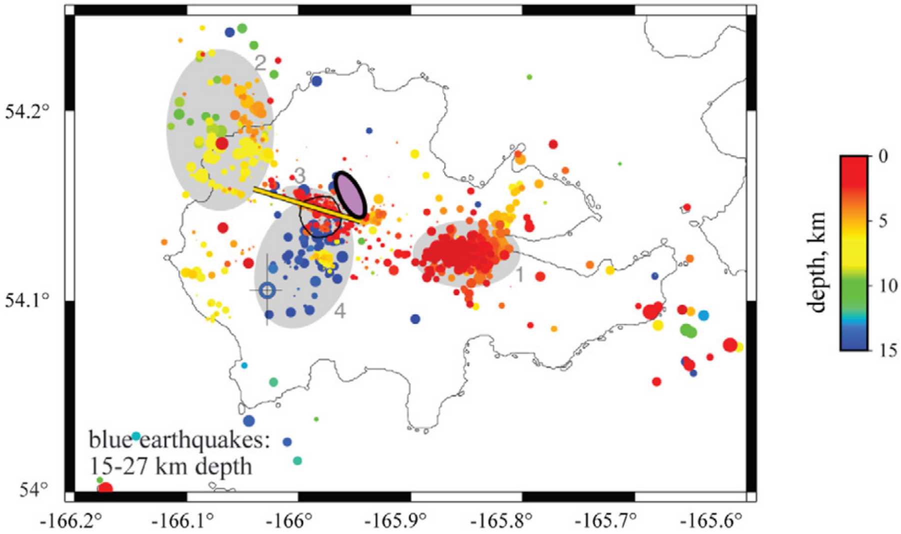

Fig. 9. Earthquake relocations from Syracuse et al. (2015) are colored according to depth. The best fit Okada model of Lu et al., 2000 is indicated with a yellow line, and the best fit Mogi model of the same work (Lu et al., 2000) is indicated with an open blue circle with error bars. The purple oval is the source location of the best fit Yang-Spheroid model for the 2008 and 2014 events. The fourth grey outlined area identified by Syracuse et al. (2015) as an area where microseismic, low-frequency temporally brief seismic swarms occurred between 2003 and 2009, which are often indicative of magma transport. Descriptions of the grey areas can be found in Section 1. Figure modified from Syracuse et al. (2015).

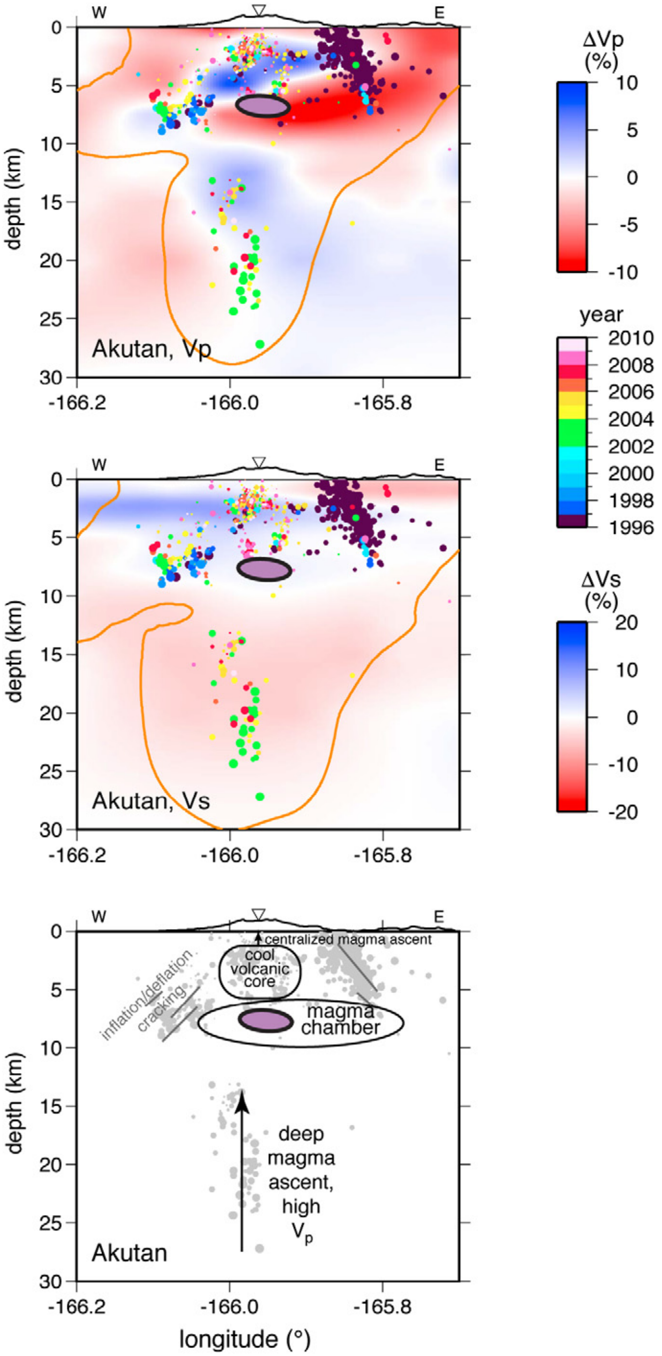

Fig. 10. Change in P and S wave velocity profiles from west to east across Akutan Caldera estimated by Syracuse et al., 2015. Red areas indicate slower velocity, corresponding to hotter, less dense material, while blue areas indicate cooler, solid, dense areas. Earthquake relocations obtained using TomoDD are plotted by size according to magnitude, and by colour according to year and the derivative weighted sums (Thurber and Eberhart-Phillips, 1999) contours are in orange, indicating the better sampled regions. The purple ellipses represent the best fit Yang-Spheroid model that was estimated using the restricted input ranges. Figure modified from Syracuse et al. (2015).

their model of a deeper magma migration zone is generally consistent with the 13 km depth Mogi source estimated by Lu et al. (2000). The failed eruption on the western flank of the volcano, modeled as a shallow dike by Lu and Dzurisin (2014), does not appear to correlate with any of the relocated seismic events. Instead the earthquake activity during 1996 is centered, not on the volcano, but farther east closer to the village of Akutan, at very shallow depths that suggest geothermal activity (Fig. 9, grey area 1).

We plot the approximate oblate spheroidal geometry and orientation for our best fit, restricted input, Yang-Spheroid model with the plot of seismic relocations (Fig. 9) and change in seismic velocity (Fig. 10) presented by Syracuse et al. (2015). When the geometry of the spheroid is projected to the surface, we see that the top of the magma source defined in this study falls into the region just northeast of the caldera and the shallow earthquakes. This projection shows that while the spheroid does not extend down, it is dipping to the southeast, towards the deeper earthquakes that are outlined in the fourth region defined by Syracuse et al. (2015) (grey area in Fig. 9) described in the introduction of this paper. This deep cluster of seismic events that occurred between 2002 and 2008 (Fig. 10 are described by Syracuse et al., 2015 as being M0.2–2.3 with no particular similarities in their waveforms, but the majority of which are low frequency events. This characterization of seismic events is often associated with the transport of magma (Aki and Koyanagi, 1981) and similar clusterings of this nature have been observed at other Aleutian volcanoes; Mount Spurr, Aniakchak, Pavlof, and Katmai complex (Power et al., 2004). The locations of these earthquakes and nature of their waveforms was the basis behind the interpretation of Syracuse et al. (2015), that there is episodic injection associated with these types of seismic signals. The pattern and depth of this interpretation is supported by the models we have presented here.

When we compare the change in seismic velocities estimated from the TomoDD inversion with our Yang-Spheroid model parameters in cross section (Fig. 10) we observe excellent spatial correlation between these two independent sets of data and models. The change in p-wave velocities (top panel, Fig. 10) indicate a hot finger extending beneath the volcano at depths of 7–10 km where Syracuse et al. (2015) interpret the hot, partially melted, aseismic, magma storage to be located. Our depths of ~6–9 km support this interpretation and tie nicely into the seismic relocation data. This pattern continues in the middle plot of Fig. 10, where we see the change in s-wave velocity values of 0, again indicating a mush setting where it is viscous enough that s-waves are not propagating, and even with the coarser resolution of the surface wave data we see the same relationship between hot, partial mush regions between 7 and 10 km and the cooler more solidified area at shallow depths. The schematic of the interpretation of Syracuse et al. (2015) (Fig. 10, bottom panel), clarifies their analysis of seismic data and allows us to show the excellent agreement between their study and the work presented here.

5.3. Volume time-series at Akutan

The method implemented here, of splitting the GPS data into five distinct time periods allows us to further define not only the geometry and orientation of magma transport and storage at Akutan volcano, but to also estimate volume change with time (Fig. 11). When a restricted input Yang-Spheroid model is used to estimate volume change through time (of the five time periods defined in this study) we see an overall accumulation of magma that amounts to 0.2 km^3 (Fig. 11). There has not been any deflation at Akutan over the duration of this study. This means that this volume of magma, 0.2 km^3 is still stored between 6 and 9 km depth below the northern flank of the volcano.

5.4. Conceptual model

Based on our best fit modeling result, and its spatial relationship to seismic events and velocities we hypothesize that the surface deformation associated with the 2008 and 2014 inflation events is a result of an increase in magma volume to a centralized, long-term storage area under the north flank of the volcano. We interpret the results from the Yang-Spheroid model not as a representation of the entirety of a source

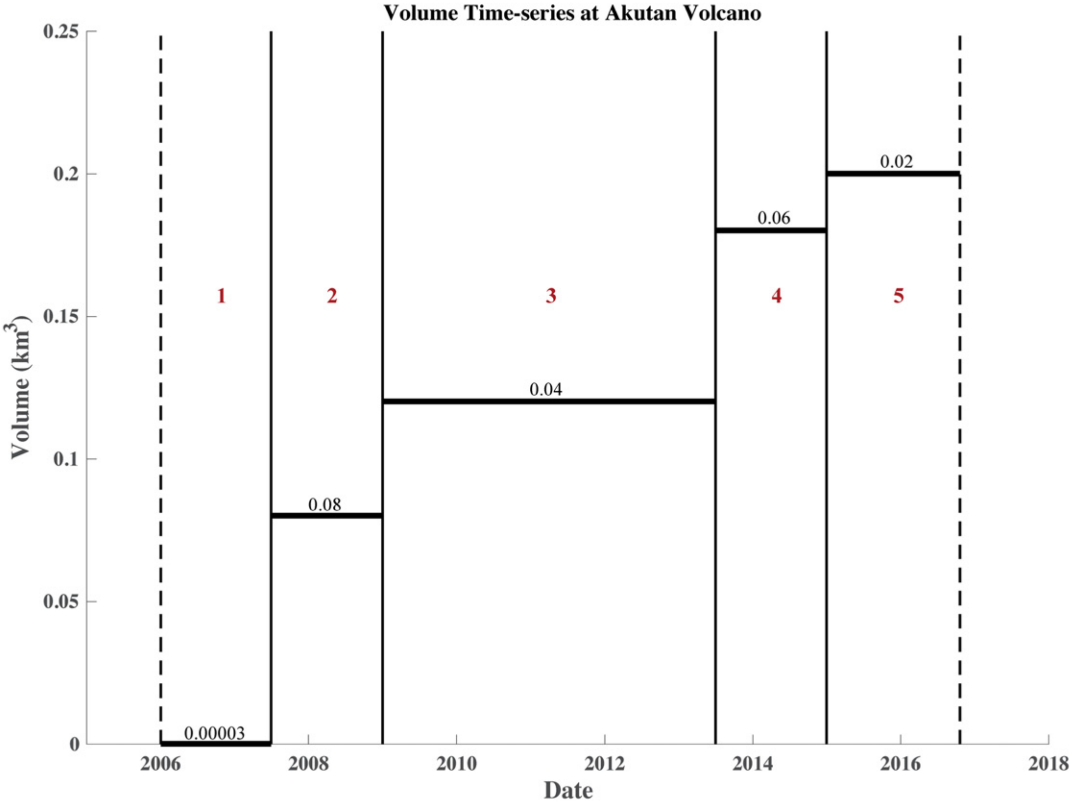

Fig. 11. Time-series evolution of volume change at Akutan volcano, with black dashed lines indicating the time periods defined in this paper (and noted by numbers 1–5). The slight deflation of the pre-2008 (1) data is evident at the beginning of this plot (0.00003 km^3). The 2008 event (2) shows the greatest amount of volume change, and while there is a steady flux (0.04 km^3) in the 2009–2014 time period (3) it is nowhere near the volume added during the shorter time periods of 2008 and 2014 (0.08 km^3 and 0.06 km^3, respectively). The 2014 inflation (4) ends abruptly in 2015 (5) and an increase in volume of only 0.02 km^3 is estimated since the 2014 event occurred, for a total accumulated volume 0f ~0.2 km^3.

chamber, but rather the active “stress-cap” to a larger region of magma and partial mush. This hypothesis is supported by the location of the earthquakes associated with the 2008 inflation period (Fig. 12). When these two independent studies are plotted together it is clear that the southern vertex of our oblate spheroid coincides with a small cluster of seismic activity during 2008. There is also a clear generalization, that seismic activity is much denser directly above our model and there is a notable void of activity directly below, again supporting our interpretation that our best fit model represents the ceiling of a larger source feature. The two 3D plots in Fig. 12 show the dynamic spatial relationship of seismicity through time and the best fit Yang-Spheroid model from the perspective of the southeastern corner looking to the northwest (Fig. 12, top) and from the south perspective looking obliquely to the north (Fig. 12, bottom). Our interpretation of this oblate spheroid as the stress cap of a chamber and not the chamber itself also makes it possible to envision the storage required to produce episodic, accumulating inflation, like that seen in 2008 and 2014. Because this inflation did not result in an eruption, and there has been no observed large scale subsidence that would be caused by a decrease in volume, we can only assume that sudden pulses cause uplift that is then maintained as the additional volume is stored in this large hot area of partial melt.

The evolution of this episodic inflation towards an eruption is not well understood, and the most recent indicator of eruptive processes at Akutan Volcano is the 1996 failed event. The subsidence on the western flank of the volcano that is evident in the model residuals and modeled by Lu and Dzurisin (2014), suggests that this area is indeed still contracting from a shallow intrusion that did not quite reach the surface. This contraction is most likely an effect of crystallization and cooling processes indicating that there was a large amount of heat flow to shallow depths in 1996. While this heat is associated with magma transport on the western flank of the volcano, in the east, this potential heat flux produced a swarm of shallow seismic activity that is indicative of increased.

hydrothermal interactions. The complicated relationship between thermodynamic properties and volume change associated with magma transport and eruptive activities is not well defined. The inflation episodes defined in this study, however, indicate that Akutan Volcano is capable of large amounts of episodic injection of magma at intermediate depths, that do not increase heat flux to the shallow geothermal regime that interacts with ground water. The island wide increase in shallow geothermal energy, seen in 1996, could potentially be used as an indicator of imminent eruptive activity, especially when associated with inflation events like those observed in 2008 and 2014.

6. Conclusions

We have presented an analysis of GPS deformation data at Akutan volcano through inversion of continuous GPS data over six time intervals for source volume change evolution. Volcanic deformation was isolated from the active tectonic displacements that are a fundamental factor when studying deformation in the Aleutians, by subtracting the horizontal components of a GPS site assumed to be far enough from the volcano that volcanic processes are not a component of its measured deformation. The inversion of this volcanic deformation through time produced an oblate spheroid of magma storage centered on the northern rim of the caldera, between the depths of 6–9 km, with axes of ~1–4 km, a strike of ~N160°E, and steep dips of ~60° from the horizontal extending southward beneath the caldera of the volcano. We conclude that this region represents the stress-cap on top of a much larger area of magma storage below, that experienced a large injection of magma ($0.08\ km^3$) over a year and a half in 2008 that was preceded by deeper seismic events (10–27 km) analyzed by Syracuse et al. (2015). A period of slower inflation that created measurable surface deformation then followed from 2009 to 2013 before another, smaller ($0.06\ km^3$), inflation event began in 2014, in the same location as the 2008 event. The GPS deformation observed here did not indicate any deflation occurring since the start of the 2008 event, so the total volume injected ($0.2\ km^3$) remains stored, likely preserving an established shallow storage of hot, partially melted, aseismic environment observed from the tomographic analysis of body and surface wave velocities (Syracuse et al., 2015). We are not able to accurately model the data following this 2014 inflation or before the 2008 event due to the small magnitudes of deformation. Additional data collection in the future should allow for better estimates of source parameters and magma volume evolution, and futures studies of the post-2014 time period can continue the time-series analysis of deformation, source parameter, and magma volume change evolution at Akutan volcano.

Supplementary data to this article can be found online at https://doi.org/10.1016/j.jvolgeores.2017.10.003.

Acknowledgements

This research was financially supported by NASA Earth and Space Science Fellowship (NNX16AO26H), NASA Earth and Surface Interior Program (NNX14AQ95G) and the Shuler-Foscue Endowment at Southern Methodist University.

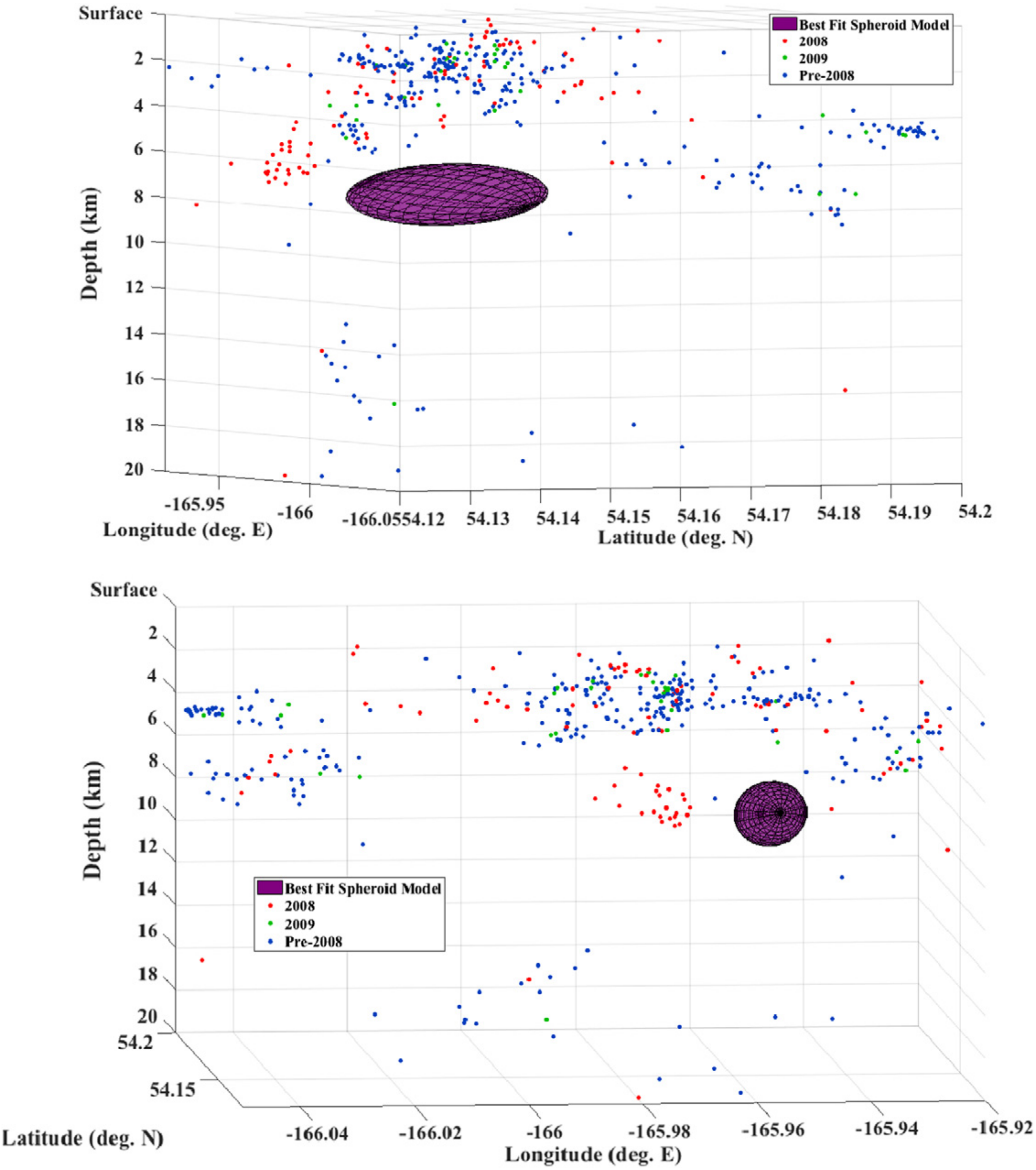

Fig. 12. Three-dimensional plot of best fit Yang-Spheroid model, with relocated seismic events from Syracuse et al. (2015). Seismic events are organized into the time periods used for the GPS data, with the entirety of the data set (1996–2009) provided by Syracuse et al. (2015). The top image is an oblique view from the southwest looking towards the northeast of the spheroid's profile, with the clear view of the 2008 seismic events relocated to the top southern vertex of the spheroid (red cluster). The bottom image is of the same dataset, from the south perspective of looking north. This view looks straight down the axis of the spheroid.

Appendix A

To better assess the validity of the tectonic estimate removed from the GPS data, this estimate was made using three different methods, and then removed two different ways. The purpose is to find the most stable tectonic estimate using GPS sites that are not contaminated by volcanic signals. Site AV15, on the eastern peninsula of Akutan island is the closest site that could provide a tectonic estimate. This site is approximately 20 km from the summit of Akutan volcano, so that any volcanic influence is expected to be minor, especially when compared with regional tectonic motion. Outside of Akutan island the neighboring island to the southwest, Unalaska (Fig. A1), provides the best opportunity for a tectonic estimate that would be valid at Akutan Island, yet not influenced by Akutan volcano. There are five available continuous GPS sites on Unalaska (AV09, DUTC, MAPS, MREP, and MSWB). Total velocity at each site was estimated using the velocity model and methods described in Section 3.1. Additionally, a linear least squares method (weighted by the uncertainty of each measurement) was used to obtain an average velocity and uncertainty for all of the continuous sites on Unalaska, this averaged velocity is referred to here as "weighted mean" (DeGrandpre, 2015). Three of the sites (MAPS, MREP, and MSWB) are located on the western flanks of Makushin volcano, and site AV09 has visibly noticeable noise, so site DUTC was also used separately as an estimate, to compare the potential input from Makushin volcano

Each of these three sets of data were then used two different ways to calculate volcanic deformation, with tectonic estimates being removed from only the horizontal (east and north) components, or by removing the tectonic estimate from all three components (east, north, vertical). The velocities for all available data for the weighted mean and DUTC estimates were used, but for the AV15 calculations, individual velocities from each of the five time periods defined in this study are used. The velocity estimations at AV15 were split up into the same time periods as the GPS observations in an effort to minimize unknown errors related to variable rates of tectonic motion and potential residual volcanic signals. This reduces theses errors to systematic errors during each time period on Akutan island. This is not done for the Unalaska sites, because they are far enough from Akutan volcano that there should be no effect, and rather are potentially being effected by Makushin volcano. The Unalaska sites could also have slightly different changes in tectonic motion, so an overall average is the simplest way to characterize the tectonic estimate using these sites.

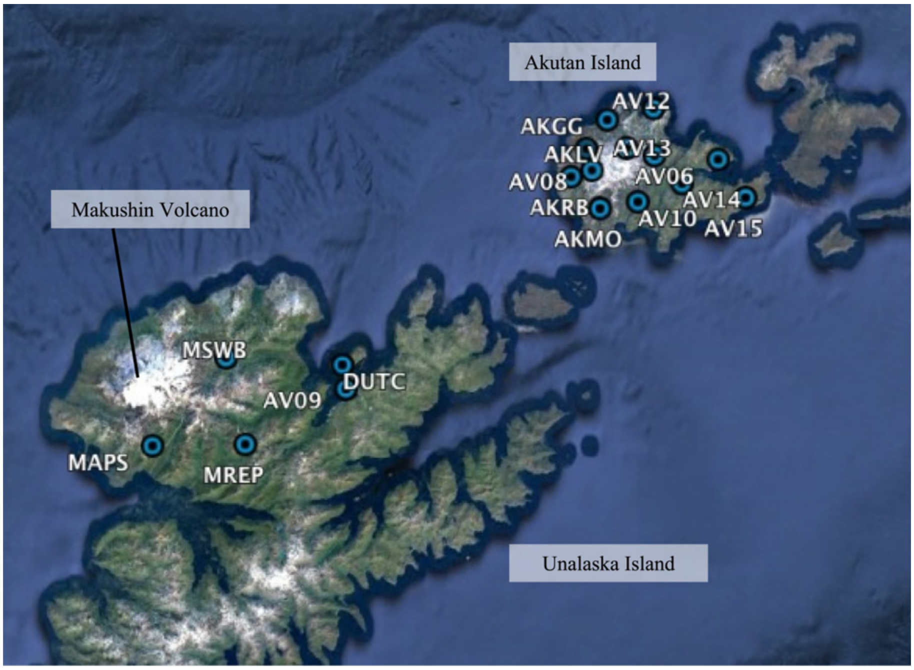

Fig. A1. Location map of Akutan island, Unalaska island, Makushin volcano, and all continuous GPS sites available on Unalaska (DUTC, AV09, MREP, MAPS, and MSWB). For a sense of scale the GPS sites on Akutan are also listed to show the dense network available in comparison to neighboring islands.

Each of these six data sets (weighted mean horizontal only, weighted mean all components, DUTC horizontal only, DUTC all components, AV15 horizontal only, AV15 all components) were modeled using the four models (Mogi, Okada, Yang-Spheroid, Yang-Ellipsoid) described in this study for each of the time periods (all, pre-2008, 2008, 2009–2013, 2014, post-2014). Only the best fit results are presented here for the 2008 and 2014 inflation events, because the other time periods are further discussed in the main paper as not being significant enough to define a best fit model. The best fit model was established using a series of F-tests following Eq. (5) and Appendix B (Table A1). Each of the data sets were best fit by a Yang-Spheroid model, for both the 2008 and 2014 inflation events. Because each tectonic estimate is different the WRSS between these data sets cannot be directly compared, and instead, to support the hypothesis that Akutan volcano is experiencing episodic inflation, we look for similarities in one data set between the 2008 and 2014 events (Fig. A2).

Table A1
WRSS values for each model during each time period using each of the six data sets. Values in bold and highlighted in yellow are the statistically significant best fit model according to F-tests performed following Eq. (5) in Section 3.1. Total number of best fit model types are indicated in the last row, showing that regardless of the data used, the Yang-Spheroid model is the best fit for both the 2008 and 2014 episodes of inflation.

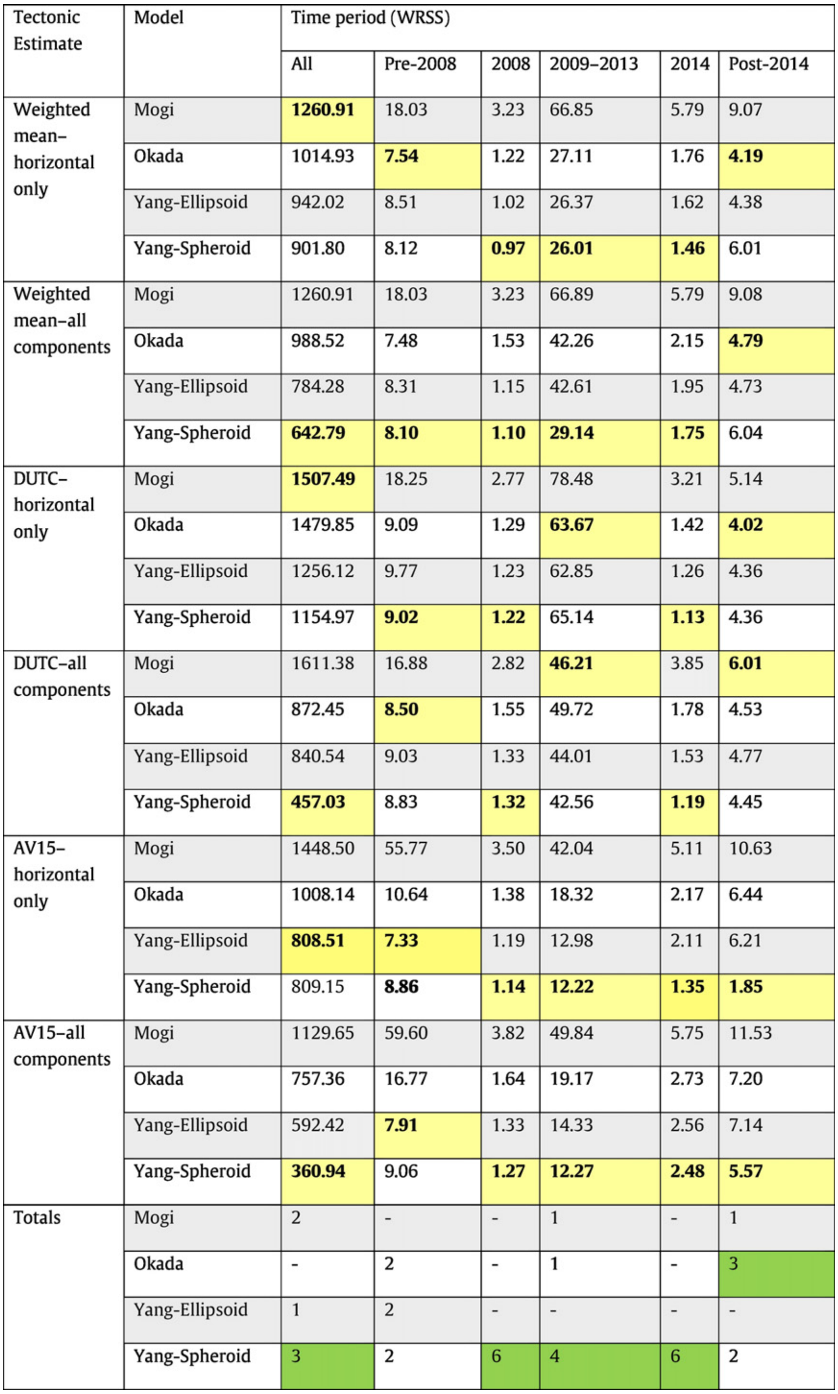

Tectonic Estimate	Model	Time period (WRSS)					
		All	Pre-2008	2008	2009–2013	2014	Post-2014
Weighted mean–horizontal only	Mogi	**1260.91**	18.03	3.23	66.85	5.79	9.07
	Okada	1014.93	**7.54**	1.22	27.11	1.76	**4.19**
	Yang-Ellipsoid	942.02	8.51	1.02	26.37	1.62	4.38
	Yang-Spheroid	901.80	8.12	**0.97**	**26.01**	**1.46**	6.01
Weighted mean–all components	Mogi	1260.91	18.03	3.23	66.89	5.79	9.08
	Okada	988.52	7.48	1.53	42.26	2.15	**4.79**
	Yang-Ellipsoid	784.28	8.31	1.15	42.61	1.95	4.73
	Yang-Spheroid	**642.79**	**8.10**	**1.10**	**29.14**	**1.75**	6.04
DUTC–horizontal only	Mogi	**1507.49**	18.25	2.77	78.48	3.21	5.14
	Okada	1479.85	9.09	1.29	**63.67**	1.42	**4.02**
	Yang-Ellipsoid	1256.12	9.77	1.23	62.85	1.26	4.36
	Yang-Spheroid	1154.97	**9.02**	**1.22**	65.14	**1.13**	4.36
DUTC–all components	Mogi	1611.38	16.88	2.82	**46.21**	3.85	**6.01**
	Okada	872.45	**8.50**	1.55	49.72	1.78	4.53
	Yang-Ellipsoid	840.54	9.03	1.33	44.01	1.53	4.77
	Yang-Spheroid	**457.03**	8.83	**1.32**	42.56	**1.19**	4.45
AV15–horizontal only	Mogi	1448.50	55.77	3.50	42.04	5.11	10.63
	Okada	1008.14	10.64	1.38	18.32	2.17	6.44
	Yang-Ellipsoid	**808.51**	**7.33**	1.19	12.98	2.11	6.21
	Yang-Spheroid	809.15	**8.86**	**1.14**	**12.22**	**1.35**	**1.85**
AV15–all components	Mogi	1129.65	59.60	3.82	49.84	5.75	11.53
	Okada	757.36	16.77	1.64	19.17	2.73	7.20
	Yang-Ellipsoid	592.42	**7.91**	1.33	14.33	2.56	7.14
	Yang-Spheroid	**360.94**	9.06	**1.27**	**12.27**	**2.48**	**5.57**
Totals	Mogi	2	-	-	1	-	1
	Okada	-	2	-	1	-	3
	Yang-Ellipsoid	1	2	-	-	-	-
	Yang-Spheroid	3	2	6	4	6	2

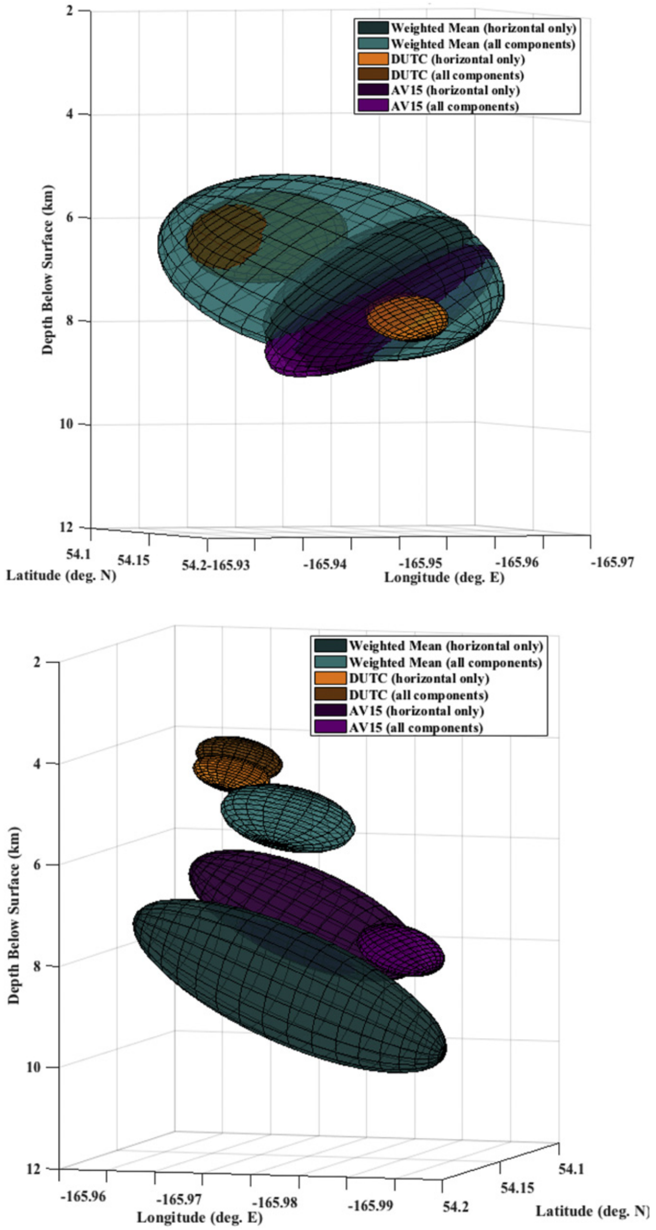

Fig. A2. Comparison of best fit models for each of the six data sets during the 2008 (top) and 2014 (bottom) inflation episodes. From Table A1 it is clear that the Yang-Spheroid best fits these events, so all of the models pictured here are created using the Yang-Spheroid model.

While these tectonic estimates are small, the effects of their variation can be seen when the best fit models for each inflation are plotted together (Fig. A2). In Fig. A2 the AV15 data, regardless of vertical adjustment, for the 2008 event are almost identical. To better understand the dynamics of the effect these tectonic estimates have on the model inversion we then compare the 2008 and 2014 events for each data set (Fig. A3). It is clear that for each data set, incorporating a vertical estimate results in a larger geometric estimate for the 2008 event (Fig. A3 and Table A2). It is also clear that the 2008 and 2014 events in the data sets that utilized GPS site DUTC have more variation than the other tectonic estimates (Fig. A3 and Tables A2 and A3). The models that are fit to data that used the weighted mean of sites on Unalaska Island as the tectonic estimate exhibit two characteristics that dissuaded us from using it in the final modeling analysis. First, the volume change and size of the 2014 event is larger than the 2008 event in the data that only removed a tectonic estimate from the horizontal components (Fig. A3 and Tables A2 and A3). Second, removing a vertical tectonic estimate resulted in dramatically different models, indicating that there are other factors contributing to this data set in at least the vertical, and potentially the horizontal. The AV15 tectonic estimate results in a larger change in volume during the 2008 than the 2014 event regardless of whether the vertical adjustment is made. Because of this stability in model results when using the AV15 data it is the tectonic estimate that is used for further modeling and interpretation in this study. The vertical velocity at AV15 was not subtracted from observed GPS velocities, because the assumption is that any vertical motion is a result of volcanic deformation and not tectonic deformation, and the larger range of variability between events when the vertical is adjusted is most likely an exaggeration.

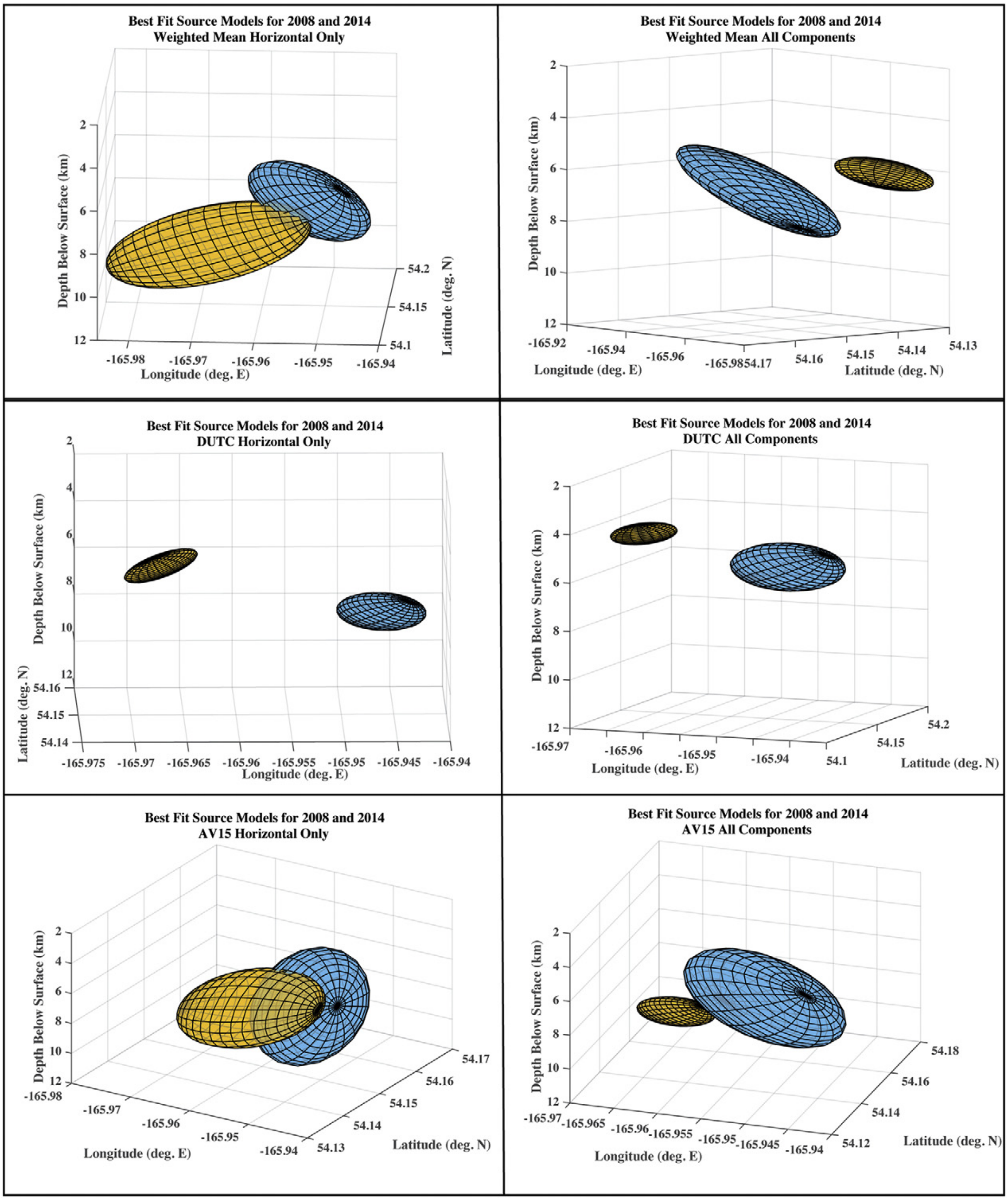

Fig. A3. Comparison of the 2008 and 2014 best fit source models for each data set. The parameters for these models can be found in Tables A2 and A3. Note the different orientation meant to maximize the viewing angle for each data set.

Table A2
Best fit parameters for each data set during the 2008 event. All parameters correspond to the results from the Yang-Spheroid model. The WRSS values of each data set cannot be directly compared, but the geometric parameters for the weighted mean and AV15 horizontal only data sets are similar, as is the respective data when all components are used.

2008 Best fit Yang-Spheroid parameters										
Data	Longitude (dec. deg. E)	Latitude (dec. deg. N)	Depth (km)	Pressure (kPa)	Length of A axis (km)	Length of B axis (km)	Strike (deg. from N)	Plunge (deg. from horz.)	Volume (km^3)	WRSS
Weighted mean–horizontal only	−165.953	54.152	7.2	3085.5	1.4	3.5	160.4	62.1	0.07	0.97
Weighted mean–all components	−165.954	54.153	6.6	325.7	4.1	3.4	160.5	55.9	0.05	1.10
DUTC–horizontal only	−165.946	54.155	8.2	15,191.6	1.0	0.9	186.2	75.6	0.04	1.22
DUTC–all components	−165.948	54.156	5.8	2396.8	2.0	1.7	186.8	50.5	0.04	1.32
AV15–horizontal only	−165.953	54.151	7.7	4008.7	1.3	3.4	165.2	63.7	0.08	1.14
AV15–all components	−165.953	54.151	7.0	360.9	3.9	3.3	165.4	57.9	0.05	1.27

Table A3
Best fit parameters for each data set during the 2014 event. All parameters correspond to the results from the Yang-Spheroid model. The WRSS values of each data set cannot be directly compared, but the geometric parameters for tall of the datasets converge on almost spherical axes lengths.

2014 Best fit Yang-Spheroid parameters										
Data	Longitude (dec. deg. E)	Latitude (dec. deg. N)	Depth (km)	Pressure (kPa)	Length of A axis (km)	Length of B axis (km)	Strike (deg. from N)	Plunge (deg. from horz.)	Volume (km^3)	WRSS
Weighted mean–horizontal only	−165.974	54.145	8.6	210.8	3.7	3.2	138.1	61.6	0.03	1.46
Weighted mean–all components	−165.969	54.148	4.8	8077.6	1.4	1.4	329.6	65.4	0.07	1.75
DUTC–horizontal only	−165.963	54.151	4.0	41,605.7	0.8	0.8	333.3	66.4	0.06	1.13
DUTC–all components	−165.963	54.150	3.7	21,760.2	0.9	0.9	334.0	69.2	0.04	1.19
AV15–horizontal only	−165.965	54.148	7.6	591.0	2.8	2.4	149.824	63.857	0.03	1.30
AV15–all components	−165.956	54.146	7.9	20,538.4	0.8	0.7	181.7	65.9	0.02	2.48

Appendix B

Best fit model parameters for each time period using each of the four deformation models were estimated (Tables B1–B4) by minimizing the calculated WRSS through a linear least squares inversion. An F-test was used to determine which of these models produced the statistically significant best fit to the deformation data (Tables B5–B7). F-tests were not performed between the Okada, Yang-Spheroid, and Yang-Ellipsoid models because they do have the same number of parameters (eight DOF) so their WRSS values can be directly compared. The statistically significant best fit models are highlighted in yellow and presented in Table B3 and B4. These best fit models are created using the input parameter ranges defined in Tables 1–3 and following methods described in Section 3.1

Table B1
Best fit Mogi model parameters. Descriptions of these parameters can be found in Section 3.3.

Data	Longitude (dec. deg. E)	Latitude (dec. deg. E)	Depth (km)	Volume (km^3)	WRSS
All	−165.942	54.161	8.7	0.019	1448
Pre 2008	−165.94	54.195	0.1	0.0002	56
2008	−165.95	54.156	5.1	0.004	3
2009–2013	−165.954	54.161	5.3	0.002	42
2014	−165.955	54.154	3.9	0.002	5
Post 2014	−165.938	54.091	9.0	0.005	11

Table B2
Best fit Okada model parameters. Descriptions of these parameters can be found in Section 3.3.

Data	Length (km)	Width (km)	Depth (km)	Dip (deg. from horz.)	Strike (deg. from N)	Longitude (dec. deg. E)	Latitude (dec. deg. N)	Opening (mm)	Volume (km^3)	WRSS
All	8.5	1.1	11.2	30.2	0.0	−166.0	54.1590	2197.47	0.021	1008.14
Pre 2008	15.0	15.0	14.3	63.8	346.4	−166.0012	54.1415	22.64	0.005	10.64
2008	0.5	3.7	9.4	19.0	286.9	−165.9443	54.1666	3931.53	0.008	1.38
2009–2013	1.5	1.0	8.9	45.3	315.2	165.9719	54.1516	3059.62	0.005	18.32
2014	0.6	3.1	8.6	22.3	268.6	−165.9567	54.1600	3090.96	0.006	2.17
Post 2014	15.0	12.9	15.0	43.0	243.8	−165.9387	54.1375	31.95	0.006	6.44

Table B3
Best fit Yang-Spheroid model parameters. Descriptions of these parameters can be found in Section 3.3.

Data	Longitude (dec. deg. E)	Latitude (dec. deg. N)	Depth (km)	Pressure (kPa)	Length of A axis (km)	Length of B axis (km)	Strike (deg. from N)	Plunge (deg. from horz.)	Volume (km^3)	WRSS
All	−165.973	54.154	7.9	36959.5	6.4	0.5	292.5	60.9	0.186	809.15
Pre 2008	−165.946	54.125	15.0	22.5	12.8	11.7	282.1	56.3	0.123	8.86
2008	**−165.953**	**54.151**	**7.7**	**4008.7**	**1.3**	**3.4**	**165.2**	**63.7**	**0.076**	**1.14**
2009-2013	**−165.966**	**54.155**	**8.6**	**34.9**	**4.9**	**4.3**	**136.6**	**57.6**	**0.010**	**12.22**
2014	**−165.965**	**54.148**	**7.6**	**591.0**	**2.8**	**2.4**	**149.824**	**63.857**	**0.030**	**1.35**
Post 2014	**−165.949**	**54.149**	**9.3**	**165.6**	**3.0**	**8.8**	**282.6**	**61.5**	**0.042**	**1.85**

Table B4
Best fit Yang-Ellipsoid model parameters. Descriptions of these parameters can be found in Section 3.3.

Data	Longitude (dec. deg. E)	Latitude (dec. deg. N)	Depth (km)	Pressure (kPa)	Length of A axis (km)	Length of B axis (km)	Strike (deg. from N)	Plunge (deg. from horz.)	Volume (km^3)	WRSS
All	**−165.964**	**54.156**	**8.3**	**61012.1**	**4.2**	**0.5**	**292.8**	**62.8**	**1.7**	**808.51**
Pre 2008	**−166.000**	**54.130**	**9.1**	**18.2**	**5.2**	**12.9**	**105.4**	**33.0**	**0.045**	**7.33**
2008	−165.952	54.152	7.9	15398.1	0.5	1.3	165.0	64.6	0.038	1.19
2009-2013	−165.956	54.161	6.9	360.9	0.5	4.0	135.9	48.4	0.009	12.98
2014	−165.956	54.148	7.5	1708.7	0.5	2.5	181.5	65.9	0.017	2.11
Post 2014	−165.938	54.126	15.0	22.2	0.5	14.7	210.2	43.8	0.008	6.21

Table B5
Comparison of statistical significance between Mogi and Okada best fit models for all data sets. F-calc values are calculated using Eq. (5), with p1 = 4 (Mogi model DOF) and p2 = 8 (Okada model DOF). The number of data points (N) represents the east, north, and vertical calculated velocities and differs between the data sets due to discontinuity at a GPS site during one or more of the designated time periods. F-crit for 95% and 99% significance are presented, with all values being a significantly better fit at the 95% confidence level, but the pre-2008 data fails at the 99% confidence level.

Data	N	WRSS (Mogi)	WRSS (Okada)	F-calc	F-crit ($\alpha = 0.05$)	F-crit ($\alpha = 0.05$)	Significant (95%)	Significant (99%)
All	36	1448.50	1008.14	3.06	2.71	4.07	Yes	No
Pre 2008	33	55.77	10.64	26.50	2.76	4.18	Yes	Yes
2008	33	3.50	1.38	9.60	2.76	4.18	Yes	Yes
2009–2013	36	42.04	18.32	9.07	2.71	4.07	Yes	Yes
2014	36	5.11	2.17	9.50	2.71	4.07	Yes	Yes
Post 2014	33	10.63	6.44	4.07	2.76	4.18	No	No

Table B6
Comparison of statistical significance between Mogi and Yang-Spheroid best fit models for all data sets. F-calc values are calculated using Eq. (5), with p1 = 4 (Mogi model DOF) and p2 = 8 (Yang-Spheroid model DOF). The number of data points (N) represents the east, north, and vertical calculated velocities and differs between the data sets due to discontinuity at a GPS site during one or more of the designated time periods. F-crit for 95% and 99% significance are presented, with all values being a significantly better fit at the 95% confidence level, but the pre-2008 data fails at the 99% confidence level.

Data	N	WRSS (Mogi)	WRSS (Yang – S)	F-calc	F-crit ($\alpha = 0.05$)	F-crit ($\alpha = 0.05$)	Significant (95%)	Significant (99%)
All	36	1448.50	809.15	5.53	2.71	4.07	Yes	Yes
Pre 2008	33	55.77	8.86	33.11	2.76	4.18	Yes	Yes
2008	33	3.50	1.14	12.95	2.76	4.18	Yes	Yes
2009–2013	36	42.04	12.22	17.09	2.71	4.07	Yes	Yes
2014	36	5.11	1.35	19.54	2.71	4.07	Yes	Yes
Post 2014	33	10.63	1.85	29.68	2.76	4.18	Yes	Yes

Table B7
Comparison of statistical significance between Mogi and Yang-Ellipsoid best fit models for all data sets. F-calc values are calculated using Eq. (5), with p1 = 4 (Mogi model DOF) and p2 = 9 (Yang-Ellipsoid model DOF). The number of data points (N) represents the east, north, and vertical calculated velocities and differs between the data sets due to discontinuity at a GPS site during one or more of the designated time periods. F-crit for 95% and 99% significance are presented, with all values being a significantly better fit at the 95% confidence level, but the pre-2008 data fails at the 99% confidence level.

Data	N	WRSS (Mogi)	WRSS (Yang – E)	F-calc	F-crit ($\alpha = 0.05$)	F-crit ($\alpha = 0.01$)	Significant (95%)	Significant (99%)
All	36	1448.50	808.51	4.27	2.73	4.11	Yes	Yes
Pre 2008	33	55.77	7.33	31.73	2.78	4.22	Yes	Yes
2008	33	3.50	1.19	9.29	2.78	4.22	Yes	Yes
2009–2013	36	42.04	12.98	12.09	2.73	4.11	Yes	Yes
2014	36	5.11	2.11	7.67	2.73	4.11	Yes	Yes
Post 2014	33	10.63	6.21	3.42	2.78	4.22	Yes	No

References

Aki, K., Koyanagi, R., 1981. Deep volcanic tremor and magma ascent mechanisms under Kilauea, Hawaii. J. Geophys. Res. 86 (B8):7095–7109. https://doi.org/10.1029/JB086iB08p07095.

Amante, C., Eakins, B.W., 2009. ETOPO1 1 Arc-minute Global Relief Model: Procedures, Data Sources, and Analysis, NOAA Tech. Memo. NESDIS NGDC-24, Natl. Geophys. Data Cent. NOAA https://doi.org/10.7289/V5C8276M.

Amoruso, A., Crescentini, L., 2009. Shape and volume change of pressurized ellipsoidal cavities from deformation and seismic data. J. Geophys. Res. Solid Earth 114 (B2).

Battaglia, M., Segall, P., Roberts, C., 2003. The mechanics of unrest at Long Valley caldera, California. 2. Constraining the nature of the source using geodetic and micro-gravity data. J. Volcanol. Geotherm. Res. 127 (3), 219–245.

Battaglia, M., Troise, C., Obrizzo, F., Pingue, F., De Natale, G., 2006. Evidence for fluid migration as the source of deformation at Campi Flegrei caldera (Italy). Geophys. Res. Lett. 33 (1).

Bonaccorso, A., 1996. Dynamic inversion of ground deformation for modeling volcanic sources (Etna 1991–1993). Geophys. Res. Lett. 23 (5), 4261–4268.

Byers Jr., F.M., Barth, T.F.W., 1953. Volcanic Activity on Akun and Akutan Island. 7th Pacific Science Conf. Proc. Auckland and Christchurch, New Zealand Vol. 2, pp. 382–397.

Davis, P.M., Hastie, L.M., Stacey, F.D., 1974. Stresses within an active volcano: with particular reference to Kilauea. Tectonophysics 22, 363–375.

DeGrandpre, K.G., 2015. Relative Sea Level Change in Western Alaska Estimated From Satellite Altimetry and Repeat GPS Measurements. Master's thesis. University of Alaska, Fairbanks ProQuest/UMI. (Publication No. 1599577).

Dzurisin, D., 2006. Volcano Deformation: New Geodetic Monitoring Techniques. Springer Science & Business Media.

Dzurisin, D., Lisowski, M., Wicks, C.W., 2009. Continuing inflation at three sisters volcanic center, central Oregon Cascade Range, USA, from GPS, leveling, and InSAR observations. Bull. Volcanol. 71 (10), 1091–1110.

Ewert, J., 2007. System for ranking relative threats of U.S. volcanoes. Nat. Hazards Rev. 8 (4):112–124. https://doi.org/10.1061/(ASCE)1527-6988.

Finch, R.H., 1935. Akutan Volcano. Z Vulkanol 16, 155–160.

Fu, Y., Freymueller, J.T., 2012. Seasonal and long-term vertical deformation in the Nepal Himalaya constrained by GPS and GRACE measurements. Journal of Geophysical Research: Solid Earth (1978–2012) 117 (B3).

Janiszewski, H.A., Abers, G.A., Shillington, D.J., Calkins, J.A., 2013. Crustal structure along the Aleutian island arc: new insights from receiver functions constrained by active-source data. Geochem. Geophys. Geosyst. 14:2977–2992. https://doi.org/10.1002/ggge.20211.

Ji, K.H., Herring, T.A., 2011. Transient signal detection using GPS measurements: transient inflation at Akutan volcano, Alaska, during early 2008. Geophys. Res. Lett. 38 L06307. https://doi.org/10.1029/2011GL046904.

Lu, Z., Dzurisin, D., 2014. InSAR Imaging of Aleutian Volcanoes: Monitoring a Volcanic Arc From Space. Vol. 411. Springer, New York.

Lu, Z., Wicks Jr., C., Power, J.A., Dzurisin, D., 2000. Ground deformation associated with the March 1996 earthquakes swarm at Akutan volcano, Alaska, revealed by satellite radar interferometry. J. Geophys. Res. 105 (B9):21,483–21,495. https://doi.org/10.1029/2000JB900200.

Lu, Z., Wicks Jr., C., Kwoun, O., Power, J.A., Dzurisin, D., 2005. Surface deformation associated with the March 1996 earthquake swarm at Akutan Island, Alaska, revealed by C-band ERS and L-band JERS radar interferometry. Can. J. Remote. Sens. 31 (1), 7–20.

McConnell, V.S., Beget, J.E., Roach, A.L., Bean, K.W., Nye, C.J., 1997. Geologic Map of the Makushin Volcanic Field, Unalaska Island, Alaska, Alaska Division of Geology and Geophysical Surveys Report of Investigations RI 97–20, Unpaged, 2 Sheets, Scale 1: 63,360. https://doi.org/10.14509/2576.

McGimsey, R.G., Neal, C., 1996. 1995 volcanic activity in Alaska and Kamchatka: summary of events and response of the Alaska volcano observatory. U.S. Geol. Survey Open-File Report 96-0738 (22 pp).

Miller, T.P., McGimsey, R.G., Richter, D.H., Riehle, J.R., Nye, C.J., Yount, M.E., Dumoulin, J.A., 1998. Catalog of the historically active volcanoes of Alaska. US Geological Survey Open-File Report 98, 582.

Mogi, K., 1958. Relations between the eruptions of various volcanoes and the deformations of the ground surfaces around them. Bull. Earthq. Res. Inst., Univ. Tokyo 36, 99–134.

Newhall, C.G., Dzurisin, D., 1988. Historical Unrest at the Large Calderas of the World (No. 1855). Department of the Interior, US Geological Survey.

Newman, A.V., Dixon, T.H., Gourmelen, N., 2006. A four-dimensional viscoelastic deformation model for Long Valley Caldera, California, between 1995 and 2000. J. Volcanol. Geotherm. Res. 150 (1), 244–269.

Okada, Y., 1985. Surface deformation due to shear and tensile faults in a half-space. Bull. Seismol. Soc. Am. 75 (4), 1135–1154.

Power, J.A., Stihler, S.D., White, R.A., Moran, S.C., 2004. Observations of deep long-period (DLP) seismic events beneath Aleutian arc volcanoes; 1989–2002. J. Volcanol. Geotherm. Res. 138:243–266. https://doi.org/10.1016/j.jvolgeores.2004.07.005.

Richter, D.H., Waythomas, C.F., McGimsey, R.G., Stelling, P.L., 1998. Geology of Akutan Island, Alaska. US Geological Survey Open-File Report 98-135.

Rivalta, E., Segall, P., 2008. Magma compressibility and the missing source for some dike intrusions. Geophys. Res. Lett. 35 (4).

Romick, J.D., Perfit, M.R., Swanson, S.E., Shuster, R.D., 1990. Magmatism in the eastern Aleutian arc: temporal characteristic of igneous activity on Akutan Island. Contrib. Mineral. Petrol. 104 (6), 700–721.

Rubin, A.M., Pollard, D.D., 1988. Dike-induced faulting in rift zones of Iceland and afar. Geology 16, 413–417.

Simkin, T., Siebert, L., 1994. Volcanoes of the World: A Regional Directory, Gazetteer, and Chronology of Volcanism During the Last 10,000 Years. 349 pp. Geoscience, Tucson, Ariz.

Syracuse, E.M., Maceira, M., Zhang, H., Thurber, C.H., 2015. Seismicity and structure of Akutan and Makushin volcanoes, Alaska, using joint body and surface wave tomography. J. Geophys. Res. Solid Earth 120:1036–1052. https://doi.org/10.1002/2014JB011616.

Thurber, C., Eberhart-Phillips, D., 1999. Local earthquake tomography with flexible gridding. Comput. Geosci. 25 (7), 809–818.

Tiampo, K.F., Rundle, J.B., Fernandez, J., Langbein, J.O., 2000. Spherical and ellipsoidal volcanic sources at Long Valley caldera, California, using a genetic algorithm inversion technique. J. Volcanol. Geotherm. Res. 102 (3), 189–206.

Waythomas, C.F., 1999. Stratigraphic framework of Holocene volcaniclastic deposits, Akutan volcano, east-central Aleutian Islands, Alaska. Bull. Volcanol. 61, 141–161.

Yang, X.M., Davis, P.M., Dieterich, J.H., 1988. Deformation from inflation of a dipping finite prolate spheroid in an elastic half-space as a model for volcanic stressing. J. Geophys. Res. Solid Earth 93 (B5), 4249–4257.

Zhang, H., Thurber, C.H., 2003. Double difference tomography: the method and its application to the Hayward Fault, California. Bull. Seismol. Soc. Am. 93 (5):1875–1889. https://doi.org/10.1785/0120020190.

Zhang, H., Thurber, C.H., 2006. Development and applications of double-difference tomography. Pure Appl. Geophys. 163:373–403. https://doi.org/10.1007/s00024-005-0021-y.